

**NASA TECHNICAL NOTE**

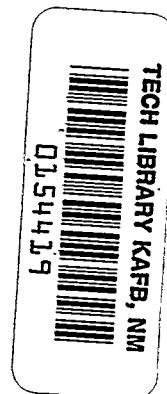


NASA TN D-2115

C.1

NASA TN D-2115

LOAN COPY: RETURN TO  
AFWL (WLL—)  
KIRTLAND AFB, N MEX



**NUMERICAL SOLUTIONS  
OF KNUDSEN FLOW ENTERING  
A CIRCULAR TUBE THROUGH  
A SMALL AXIAL ORIFICE**

*by Edward A. Richley and Carl D. Bogart*

*Lewis Research Center  
Cleveland, Ohio*

**NUMERICAL SOLUTIONS OF KNUDSEN FLOW ENTERING A  
CIRCULAR TUBE THROUGH A SMALL AXIAL ORIFICE**

**By Edward A. Richley and Carl D. Bogart**

**Lewis Research Center  
Cleveland, Ohio**

**NATIONAL AERONAUTICS AND SPACE ADMINISTRATION**

**For sale by the Office of Technical Services, Department of Commerce,  
Washington, D.C. 20230 -- Price \$1.25**



NUMERICAL SOLUTIONS OF KNUDSEN FLOW  
ENTERING A CIRCULAR TUBE THROUGH  
A SMALL AXIAL ORIFICE

SUMMARY

The problem of determining Knudsen flow flux distributions in certain models pertinent to electric rocket thruster design is discussed. A basic model of circular cross section is established in which particles are assumed to enter one end through a small orifice and leave the other end, which is wholly open.

Analyses are given for the cases of diffuse and specular reflections from the walls. For diffuse reflection, the resulting integral equations are solved by an iterative procedure on an IBM 7094 computer. Flux distributions are presented for the rear wall, the side wall, and the open end of the basic model. For the case of specular reflection, approximate solutions are obtained by a method of ray tracing. The specular-reflection analysis is extended to complex models that closely approximate five variations of an electron-bombardment ion thruster. Flux distributions for these models are found to be relatively insensitive to changes in propellant-distributor geometry.

INTRODUCTION

The subject of rarefied gas dynamics is receiving greater attention in recent years, largely because of the intense interest in exploration of outer space. In the study of electric propulsion, for example, a knowledge of the arrival rate per unit area, or flux distribution, of rarefied gases is of value in predicting thruster performance. In general, a limited number of solutions to flux-distribution problems is available in the literature. Solutions are largely dependent on the assumed mode of surface reflection and on the geometry of the model under consideration.

The study of free-molecule flow, or Knudsen flow, in tubes of right-circular cross section has perhaps received the most attention and dates back to the early work of Knudsen and Clausing. More recently several others have investigated this problem. Solutions to the "infinite tube" problem are available in most texts on kinetic theory (e.g., ref. 1). Solutions of efflux patterns from short tubes are presented in reference 2. In reference 3, perhaps the most comprehensive work of recent date on the Knudsen flow problem, the tube flow problem, among many others, is discussed. Other investigators have studied special variations of the tube flow problem. For example, in reference 4, the problem of determining the pumping speed of a circular aperture in a diaphragm across an in-

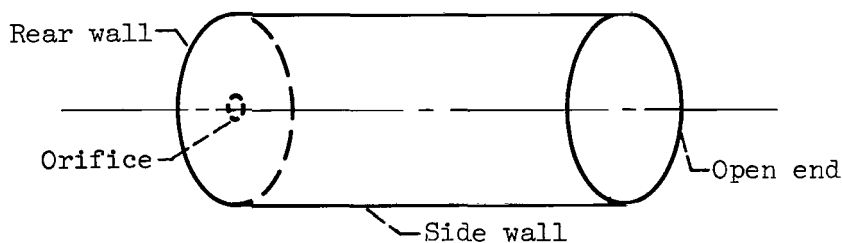
finite tube is studied. Recently, solutions for molecular-flow flux distributions in right-circular tubes (ref. 5) and in tapered tubes (ref. 6) have been presented.

Particle behavior in the free-molecule flow regime is of interest in the field of electric propulsion because, frequently, propellant-mass flow rates in electric rocket thrusters are such that particle densities are very low. Determining the flux distributions of interest, however, is seldom a straightforward matter. An electrostatic ion thruster that exemplifies the problem is shown in figure 1. Details of its operation and performance were first reported in reference 7 and will be mentioned here briefly for orientation purposes only. Neutral propellant vapor passes from the vaporizer, through an orifice, and into the ion chamber. The propellant is ionized and a plasma is formed. By virtue of a potential difference maintained between the screen and the accelerator grid, ions are extracted, accelerated, and exhausted.

The purpose of this report is to determine the neutral-particle flux distributions of certain axisymmetric models that arise in connection with this ion-thruster configuration. Two analyses are made of a model consisting of a right-circular cylinder in which particles enter at one end through a small orifice on the axis and leave the downstream end, which is wholly open. The difference between the two analyses stems from the mode of surface reflection assumed: diffuse or specular. Solutions of flux distributions are obtained on an IBM 7094 computer. Because of its relative simplicity, the specular-reflection analysis is extended to models that are representative of the ion-thruster configuration discussed.

#### MODEL AND ASSUMPTIONS

The basic model from which the two analyses are developed is shown in sketch (a).



(a)

Particles enter the right-circular, cylindrical enclosure through a small, thin orifice located on the axis at the rear wall. The source of the entering particles is considered to be a large chamber in which the gas is in equilibrium. The entering particle flux is assumed uniform across the orifice opening. The pressure downstream of the open end is assumed zero except for that contribution that arises from the leaving particles. In one analysis, reflections from the walls are assumed diffuse; in the other, specular. In both analyses, the entering flux from the orifice is assumed to follow the cosine law distribution and

the particle arrival rate at the walls is assumed equal to the leaving rate. The particle mean free path is assumed sufficiently large to ensure free-molecule flow everywhere within the model.

Full consideration of the exact nature of the surface-reflection process is beyond the scope of this report. Reference 8 suggests that the occurrence of specular reflection (wherein the angle of reflection of a particle leaving a surface equals the angle of incidence) is unlikely. Reference 9, however, points out that specular reflection may be of practical importance in very high speed flows. It is generally agreed among experts that diffuse reflection (wherein the direction of reflection of a particle from the surface is unrelated to the direction of incidence) is the more probable mode.

## ANALYSES AND PROCEDURES

### Fundamental Relations

The analyses to be discussed are based on fundamental relations developed from elementary kinetic theory.

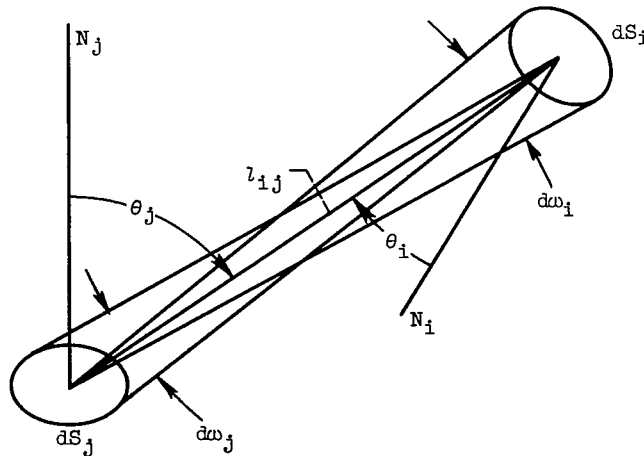
The rate of particle flow from a differential area  $dS_i$  in a direction  $\theta_i$  arriving at an area  $dS_j$  is

$$d(\bar{n}_{ij}) = n_i \bar{v}_i \cos \theta_i dS_i \frac{d\omega_j}{4\pi} \quad (1)$$

where  $\bar{v}_i$  is the isotropic mean particle speed,  $n_i$  the particle density, and

$$d\omega_j = \frac{\cos \theta_j dS_j}{l_{ij}^2} \quad (2)$$

(All symbols are defined in appendix A.) The subscript notation is described in sketch (b).



(b)

(2), The arrival rate, or flux, at  $dS_j$  from  $dS_1$  is, from equations (1) and

$$d(\dot{n}_j) = \frac{d(\bar{n}_{1j})}{dS_j} = \frac{1}{4} n_1 \bar{v}_1 \cos \theta_1 \cos \theta_j \frac{dS_1}{\pi l_{1j}^2} \quad (3)$$

With  $\dot{n}_1 = (1/4)n_1\bar{v}_1$ , equation (3) can also be written as

$$d(\dot{n}_j) = \frac{\dot{n}_1}{\pi} \cos \theta_1 \cos \theta_j \frac{dS_1}{l_{1j}^2} \quad (4)$$

From equation (4), the flux through a differential area  $dS_h$  of a hemisphere of radius  $l_h$ , from a small orifice centrally located on the base, can be written as

$$d(\dot{n}_h) = \frac{\dot{n}_1 A_1}{\pi l_h^2} \cos \theta_1 = \frac{\bar{n}_1}{\pi l_h^2} \cos \theta_1 \quad (5)$$

In equation (5), the  $\cos \theta_1 = 1$ , and the orifice area  $A_1$  is considered small enough to be almost a point source, that is,  $A_1 \ll \pi l_h^2$ .

Equation (4) is the basic relation from which the subsequent analyses are developed. It will be used as written for the diffuse-reflection analysis and as rewritten in the form of equation (5) for the specular-reflection analysis.

#### Diffuse-Reflection Analysis

In formulating the problem described herein, a set of two simultaneous integral equations arises from considering the contributions from all sources to the local arrival rate (assumed equal to the leaving rate) on each surface.

The equations that describe these local fluxes are given next in general form and are derived in detail in appendix B. Model surfaces and pertinent variables are identified in figure 2. The local flux on the rear wall  $\dot{n}_4(r_4)$  includes contributions from all local points on the side wall and can be expressed as

$$\dot{n}_4(r_4) = \int_0^L \dot{n}_3(x) F(x, r_4) dx \quad (6)$$

(rear wall)                      (side wall)

On the side wall the local flux  $\dot{n}_3(x_3)$  includes contributions from the orifice, the rear wall, and the side wall itself:

$$\dot{n}_3(x_3) = \dot{n}_1 G(x_3) + \int_{d_1/2}^R \dot{n}_4(r) H(r, x_3) dr + \int_0^L \dot{n}_3(x) I(x, x_3) dx \quad (7)$$

(side wall)
(orifice)
(rear wall)
(side wall)

The local flux in the plane of the open end  $\dot{n}_2(s_2)$  includes contributions from the orifice, the rear wall, and the side wall:

$$\dot{n}_2(s_2) = \dot{n}_1 J(s_2) + \int_{d_1/2}^R \dot{n}_4(r) K(r, s_2) dr + \int_0^L \dot{n}_3(x) M(x, s_2) dx \quad (8)$$

(open end)
(orifice)
(rear wall)
(side wall)

In these equations, the functions  $F$ ,  $G$ ,  $H$ ,  $I$ ,  $J$ ,  $K$ , and  $M$  are the kernel functions of the model geometry (see appendix B). The side wall is the wall of the cylinder. The flux entering through the orifice,  $\dot{n}_1$ , is assumed known, that is, a constant.

Equations (6) and (7) must be satisfied in order to obtain a solution to equation (8). The basic difficulty encountered in seeking solutions to equations (6) and (7) stems from the fact that the functions  $\dot{n}_3(x)$  and  $\dot{n}_4(r)$  - the flux distributions along the side and rear walls, respectively - are unknown. Thus, direct integration is not possible.

Described in reference 10 is a numerical method of solution to the problem of determining the thermal-radiation characteristics of cylindrical cavities. The simultaneous integral equations for the apparent emissivity distribution that are given in reference 10 are similar in structure to equations (6) and (7). The procedure followed herein to obtain solutions to equations (6) and (7) employs techniques similar to those used in reference 10. Solutions are obtained by iterative numerical integration performed on the IBM 7094 computer of the NASA Lewis Research Center.

#### Diffuse-Reflection Procedure

For actual computation, equations (6) and (7) are first normalized by dividing through by  $\dot{n}_1$ , the flux through the orifice. To start the iterative method of solution, an initial guess is made of the flux distribution  $\dot{n}_3(x)$  in equation (6). The significance of the value chosen for the initial guess of  $\dot{n}_3(x)$  will be discussed later in this section. The function  $\dot{n}_4(r_4)$  is then calculated by supplying values of  $r_4$ ,  $d_1/2 \leq r_4 \leq R$  to the integrand function, for instance  $f(x, r_4) = \dot{n}_3(x) F(x, r_4)$ , and then by numerically integrating  $f(x, r_4)$  by Simpson's rule to obtain pointwise values.

To obtain values of  $\dot{n}_3(x_3)$  from equation (7), a similar procedure is fol-

lowed using the values of  $\dot{n}_4(r)$  produced from equation (6) and the initial guess of  $\dot{n}_3(x)$ . Values of  $x_3$ ,  $0 \leq x_3 \leq L$  are supplied in G, H, and I of equation (7). The function G is prescribed: the integrand of the first integral becomes a function, for instance,  $h(r, x_3)$ ; and the integrand of the second integral becomes a function, for example,  $i(x, x_3)$ . The functions  $h(r, x_3)$  and  $i(x, x_3)$  are numerically integrated, added to  $G(x_3)$ , and values of  $\dot{n}_3(x_3)$  are thus obtained. The newly tabulated  $\dot{n}_3(x)$  function is then used as the "next guess" in equation (6) and the cycle is repeated until convergence is obtained, that is, until the values of  $\dot{n}_3(x)$  obtained from equation (7) agree with the values of  $\dot{n}_3(x)$  supplied previously in equation (6).

With the flux distributions,  $\dot{n}_3(x)$  along the side wall and  $\dot{n}_4(r)$  along the rear wall, determined, the values of the local flux distribution,  $\dot{n}_2(s_2)$ , across the open end can then be determined by numerical integration of equation (8). No iteration is required in this case; however, the integration must be done once for each value of the radius,  $s_2$ .

For the iterative integration of equations (6) and (7), the  $r$  and  $x$  increments used were as follows: on the rear wall,  $1/42$  of the cylinder radius; on the side wall,  $1/40$  of a unit length; and, on the open end,  $1/40$  of the cylinder radius. The increment used on the rear wall was chosen because the Simpson's rule integration requires an even number of increments. In the first integral of equation (7), the  $r$  integration is carried out from  $d_1/2$  to  $R$ . With  $d_1/2R = 1/21$ , 40 increments were available. The second integral of equation (7) was broken into either two or three parts, depending on whether the  $x_3$  point being calculated was numbered odd or even. When  $x_3$  was an odd-numbered point, an even number of increments was available to the left and right of  $x_3$  and Simpson's rule integration was applicable. When  $x_3$  was an even-numbered point, Simpson's rule integration was applied over the range from  $x = 0$  to the  $x$  step value preceding the  $x_3$  point, and from the  $x$  value after the point out to  $x = L$ . Over the interval between, trapezoidal integration was applied.

Because of the complex structure of equations (6) and (7), trial solutions were investigated in an attempt to establish convergence criteria and overall accuracy of the results.

To determine the effect of the initial guess of the  $\dot{n}_3(x)$  function that must be supplied in equation (6) to start the iterative procedure, several different functions were investigated. Functions that had positive slopes, negative slopes, and even a value of zero, were tried. In all cases, convergence to the same final answers was indicated. No stability problems were encountered; however, the rate of convergence depended on the particular initial guess selected. The number of iterations required for the final solutions was reduced to low values (as indicated in table I) by noting that the constant-slope portion of the side-wall relative-distribution curves could be approximated by an initial guess of  $\dot{n}_3(x)/\dot{n}_1 \approx 0.001\{[(L/R) + 1] - (x/R)\}$ .



The "ratio test" indicated in table I constitutes a check on the numerical results from the law of mass conservation. This check ratio is derived from a comparison of the flow in through the orifice and the flow out through the open end plus the small fraction returning back through the orifice. Because of the area ratios, this latter fraction would be expected to be small. Expressed mathematically, the comparison is

$$2\pi \int_0^{d_1/2} \dot{n}_4(r) r \, dr + 2\pi \int_0^R \dot{n}_2(s) s \, ds = \dot{n}_1 \pi \left(\frac{d_1}{2}\right)^2 \quad (9)$$

or, in terms of relative flux distributions,

$$\int_0^{d_1/2} \frac{\dot{n}_4(r)}{\dot{n}_1} r \, dr + \int_0^R \frac{\dot{n}_2(s)}{\dot{n}_1} s \, ds = \frac{1}{2} \left(\frac{d_1}{2}\right)^2 \quad (10)$$

For exact agreement, a ratio of the left side to the right side of equation (10) should equal unity. To make the desired comparison it is necessary to calculate the "return-flux" distribution across the orifice opening from equation (6) and then perform the integration indicated in equation (10). A trial calculation for a length to radius ratio ( $L/R$ ) of 5 gave a return-flux ratio of 0.0046 and an open end ratio of 0.9713, which is a total of 0.9759. Although numerical integration that involved several integrals was required to obtain this ratio, the result seems very good. Other trial solutions showed that this degree of agreement was not possible with coarser increments, while the use of finer increments resulted in little or no improvement and added greatly to machine computation time. Since the return-flux ratio was negligible by comparison and calculation also required additional computer time, it was neglected in obtaining the final solutions.

As a result of the preliminary evaluations discussed, a convergence criterion was established for the final runs and consisted of the following two checks:

(1) After 20 iterations of equations (6) and (7), equation (8) was solved. The flux distribution was then integrated as in equation (10), and a ratio of the left side to the right side was formed. If the ratio obtained was greater than an arbitrarily selected value - either 0.96 or 0.97 was used - then the iterative procedure was stopped and the results were listed. It was necessary to decrease the value of the comparison ratio as the length to radius ratio increased because of inherent inaccuracies of the numerical integration.

(2) If the ratio obtained in item (1) was less than the preassigned value, an additional 20 iterations were performed on equations (6) and (7) and a new ratio comparison was made. If the condition of item (1) was satisfied, the results were listed. If not, the ratio obtained was compared with the ratio of the previous 20 iterations. If the change in the ratios compared was not greater than 0.0001, iteration was stopped, and the results were listed. Otherwise an-

other 20 iterations were accomplished and new comparisons were made.

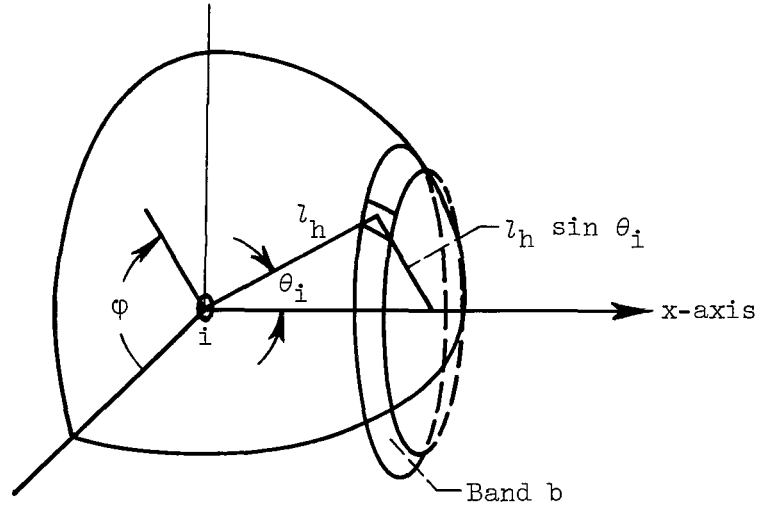
As a precaution to prevent endless iteration if the ratio test failed, the program was to be stopped after 100 iterations and the results listed. In the final solutions that employed the initial guess given previously, this precaution was not needed.

### Specular-Reflection Analysis

An approximate method of solution of the specular-reflection problem was developed that is readily adaptable to numerical techniques.

If equation (5) is multiplied through by  $dS_h$ , where, from sketch (c),  $dS_h = l_h^2 \sin \theta_i d\theta_i d\varphi$ , the result is

$$d(\bar{n}_h) = \frac{\bar{n}_1}{\pi} \cos \theta_i \sin \theta_i d\theta_i d\varphi \quad (11)$$



(c)

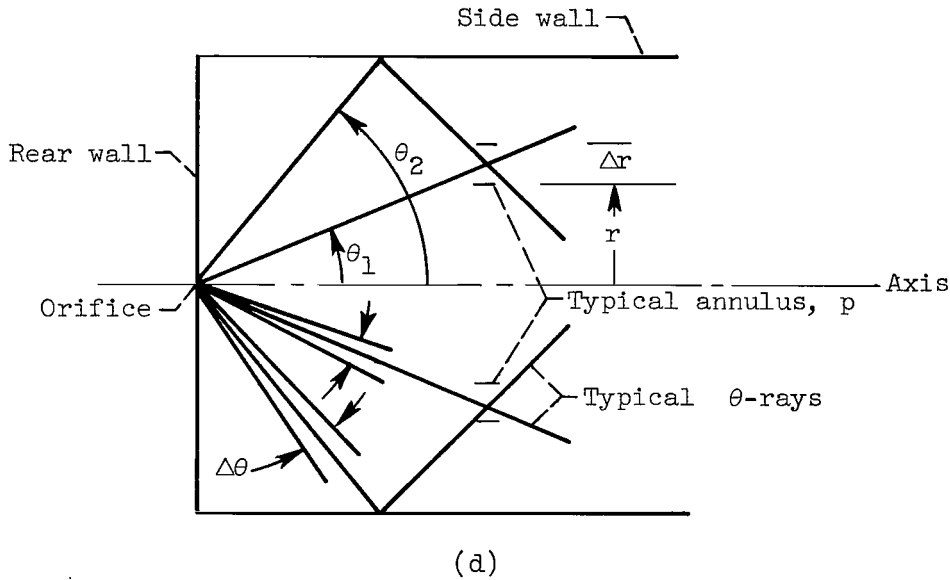
In equation (11),  $d(\bar{n}_h)$  is the arrival rate (particles per unit time) on the differential element of the hemisphere. The arrival rate passing through a differential band is

$$\begin{aligned} d(\bar{n}_b) &= \frac{\bar{n}_1}{\pi} \int_0^{2\pi} \cos \theta_i \sin \theta_i d\theta_i d\varphi \\ &= \bar{n}_1 2 \cos \theta_i \sin \theta_i d\theta_i \\ &= \bar{n}_1 \sin 2\theta_i d\theta_i \end{aligned} \quad (12)$$

For the analysis, it is assumed that the particles initially leaving the orifice in a direction near and about  $\theta_1$  are restricted always to follow the direction traced by the "ray" associated with  $\theta_1$ . The arrival rate (particles per unit time) on an arbitrarily narrow band on the hemisphere (sketch (c)) is then written from equation (12) as

$$\Delta \bar{n}_b \approx \bar{n}_1 \sin 2\theta_1 \Delta\theta_1 \quad (13)$$

To find the flux (particles per unit area per unit time) through an annulus, such as shown in sketch (d), it is necessary to sum the arrival-rate contribu-



tions from all rays passing through the annulus and to divide by the area of the annulus, that is,

$$\dot{n}_p \approx \frac{\sum \Delta \bar{n}_b}{A_p} \quad (14)$$

Substituting equation (13) into equation (14) and noting that  $A_p = \pi[(r + \Delta r)^2 - r^2]$  yield

$$\dot{n}_p \approx \frac{\bar{n}_1 \Delta\theta \sum_{i=1}^j \sin 2\theta_i}{\pi \Delta r (2r + \Delta r)} \quad (15)$$

The summation  $i$  through  $j$  includes all rays passing through the annulus.

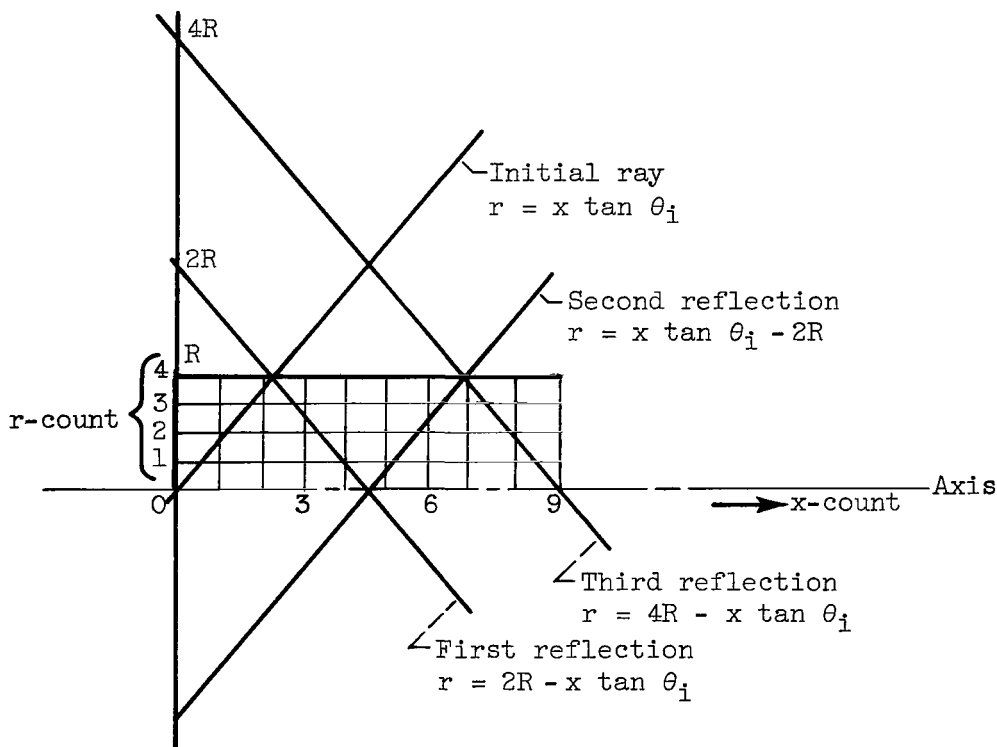
An alternate approach to the specular-reflection problem was suggested by

Eli Reshotko of Lewis and is given in appendix C. Although the method yields an analytic expression for the flux distribution across the open end of the basic model, it is not readily extended to handle more complex models. Agreement of results between the two methods for the basic model, however, indicates that the method used herein can reasonably be extended to more complex geometries.

### Specular-Reflection Procedure

The flux calculation which is largely a matter of bookkeeping, was accomplished using the IBM 7094 computer. For the model shown in figure 2, a mesh was overlayed. The mesh size used in the  $r$ -direction prescribed the values for the denominator of equation (15) for each annulus. The value of  $\Delta\theta$  is prescribed by dividing the rays that emerge from the orifice and range in value from zero to  $\pi/2$  into an arbitrary number of rays such that the first ray is  $\Delta\theta/2$ , the next is  $[(\Delta\theta/2) + \Delta\theta]$ , the next is  $[(\Delta\theta/2) + 2\Delta\theta]$ , and so on.

The procedure is begun by following the first ray throughout its entire path and noting the  $r$ -count location at each  $x$ -count and storing this information. The next ray is then followed and its path recorded in a similar manner. When a ray arrives at the side wall it is reflected, the angle of reflection being set equal to the angle of incidence. In the same manner, the rays, which are actually representative of cones, are reflected from the axis. Thus, it is possible to accomplish the entire calculation by following rays in the  $r, x$  plane. For example, the  $r$ -count position of the initial ray at any  $x$ -count position (see sketch (e)) is given by  $r = x \tan \theta_1$ .



(e)

These position values are recorded as the x-count is increased in steps until the value  $r = R$  is reached. The equation of the first reflection is  $r = 2R - x \tan \theta_1$ , and the procedure of storing r-count locations of  $\theta_1$ , as the x-count is increased, is continued until the value of  $r = 0$  is reached. The ray is reflected from the axis, the equation of the second reflection being  $r = x \tan \theta_1 - 2R$ . The equation of the third reflection is  $r = 4R - x \tan \theta_1$ , and so on. With each reflection from the wall  $r = R$ , the sign of the  $x \tan \theta_1$  component alternates from positive to negative, and the  $R$  component increases by  $2R$ . With each reflection from the axis, the sign alone alternates. In this manner, the rays  $\theta_{1 \rightarrow j}$  passing through a given r-count location are recorded, and after completing the tracing of all rays, equation (15) may be applied at the x-planes of interest.

Flux distributions on the side wall can be obtained in a similar manner by counting and storing ray information in x-count locations at  $r = R$  and then dividing by the incremental cylinder surface area  $2\pi R \Delta x$ .

Because of questions previously discussed concerning the plausibility of the specular reflection process as well as recognition of the approximation of the method, the discussion on the accuracy of the method is confined to the details of the calculation itself. The assumption that rays initiate on the axis at the plane of the rear wall obviously excludes application of the method to problems other than those in which the orifice diameter is very small compared with the cylinder diameter.

The accuracy of the calculation is strongly dependent on the size of the  $\Delta\theta$  increment and somewhat less dependent on the size of the  $\Delta r$  increment. The integral over  $\theta$  in equation (12) is equal to unity and the summation over  $\theta$  given in equation (15) approximates this integral. For example, if  $R$  were divided into 10 increments, while at the same time the  $\Delta\theta$  increment was selected to be  $45^\circ$  (two rays), there would be several locations through which no ray would pass. Also, if only two rays were used ( $\Delta\theta = 45^\circ$ ,  $\theta_1 = 22.5^\circ$ ,  $\theta_2 = 67.5^\circ$ ), the summation over  $\theta$  would equal 1.112. Therefore, to include all locations and to obtain a good approximation of the integral, it is desirable to choose  $\Delta\theta$  as small as is practical. Optimization of the  $\Delta\theta$  increment and  $\Delta r$  increment was investigated. It was found that a  $\Delta r$  increment of from 20 to 25 units of  $R$ , used in conjunction with a  $\Delta\theta$  increment of  $0.125^\circ$  (i.e., 720 rays), gave good results - measured in terms of the degree of "smoothness" of the distribution curves. With this choice of  $\Delta\theta$ , the summation over  $\theta$  equals unity to five significant figures. A  $\Delta\theta$  increment of  $0.0125^\circ$  (i.e., 7200 rays) was investigated and was found to have little effect on the results.

It is apparent from inspection of both the diffuse- and specular-reflection equations that flux distributions are dependent only on the cylinder length to radius ratio. All results to be presented have thus been normalized by the cylinder radius,  $R$ .

## RESULTS AND DISCUSSION

### Diffuse Reflection

Values of the relative flux distribution along the rear wall, the side wall, and the open end of the model shown in figure 2 were obtained for cylinder length to radius ratios of 1, 2, 3, 4, 5, and 10. The orifice to cylinder radius ratio in all cases was 1/21. Results are plotted in figures 3 to 5, and some tabulated values are given in tables I and II. These values are given to three significant figures, although machine computation gave eight.

Turning first to the results shown in the figures, it is seen from figure 3 that the distributions on the rear wall for various  $L/R$  are similar in form and differ primarily in magnitude. The flux-distribution curves across the open end (fig. 4) approach the shape of the infinite-tube-distribution curve (ref. 1) as the  $L/R$  increases. In making this comparison, the infinite tube distribution from reference 1 has been normalized to the  $L/R = 10$  value on the axis. The distributions in figure 4 are quite similar for length to radius ratios greater than two. Inspection of the distributions of figure 4 indicates that, as would be expected, the total relative arrival rates at the open end are nearly equal to unity for all  $L/R$  solutions (see table I).

The flux-distribution curves along the side wall, given in figure 5, are all similar, each exhibiting an initial increase followed by a uniform decrease as  $x/R$  increases. As mentioned in the Diffuse-Reflection Procedure section, it was found that the constant-slope portion of these curves beyond the peak is closely approximated by the relation  $\dot{n}_3(x)/\dot{n}_1 = 0.001\{[(L/R) + 1] - (x/R)\}$ .

Because of the steep slope of the curves at the intersections of surfaces, end-point values of the curves of figures 3 to 5 are not shown in the figures but are given in table II. Values at the intersections of surfaces, for example,  $\dot{n}_4(R)$  and  $\dot{n}_3(0)$  are different. The mathematical reason for these differences cannot be rigorously explained from equations (6) and (7) but is somewhat apparent if the equations are compared, for example, for values of  $r_4 = R$  and  $x_3 = 0$ , respectively. At this point, the equations become similar in form, but each contains a different kernel function. In reference 10, it was found that similar differences in corner values occurred in solutions to the problem of apparent emissivity of a cylindrical cavity. The opinion expressed in reference 10 is that the finding seems physically reasonable, based on the idea that an observer approaching the corner along the side wall would have a different view from that of an observer approaching the corner along the rear wall. A similar idea may apply to the problem herein.

Extending the diffuse-reflection analysis to models such as that represented by the electron-bombardment thruster shown in figure 1, wherein a distributor and screen grid are included, poses a formidable problem. The governing integral equations may be readily written; however, instead of two equations, three or more arise (some of which contain integrals having variable limits of integration) that must be simultaneously satisfied. While solution by the iterative method is possible in principle, it may be much more difficult to accomplish practically because of the additional number of unknown distribution functions

involved. The iterative procedure can no longer be initiated with a guess of only one unknown distribution function.

### Specular Reflection

Values of the relative flux distribution across the open end of the basic model of figure 2 are given in figure 6(a). These results may be compared with the results for diffuse reflection given in figure 4. Both sets of curves show maximums in the center (axis) and minimums near the wall; however, the portion of the curves between have opposite curvatures. The shape of the "specular" curves was nearly the same for all cases investigated. In this model, particles proceed in the forward direction only, so that the flux distribution on the rear wall is zero.

Values of the open-end distribution determined from the approximate method (eq. (15)) are compared with those of the analytic method (eq. (C5)) in figure 6(b) for an  $L/R$  of 5. In determining values from equation (C5), 100 terms were used (i.e.,  $\alpha = 100$ ). It can be seen from figure 6(b) that the results from the approximate method compare quite well with the analytic results. Values for an  $L/R$  of 1 determined from equation (C5) were practically identical with those determined from equation (15). As mentioned earlier, the analytic method is useful for comparative purposes but cannot be easily extended to more complex models.

A side-wall distribution for an  $L/R$  of 4 is shown in figure 7 and compared with the diffuse-reflection distribution. The variation of the specular-reflection curve with  $x/R$  is typical of those obtained with other  $L/R$  values.

This method of analysis was also applied to models representative of the electron-bombardment thruster shown in figure 1. Ion-chamber pressures in this thruster have been estimated to be of the order of  $10^{-4}$  millimeter of mercury. The thruster uses mercury vapor as a propellant. The mean free path of the mercury atom at this level of pressure with thermal equilibrium assumed is approximately 25 centimeters compared with chamber dimensions of about 10 centimeters. It is likely, therefore, that molecular flow occurs in the chamber. Thermal environment and the ionization processes, however, could have an appreciable effect on the flow.

Various propellant "distributors" have been tested in this thruster in an effort to alter neutral propellant distribution and improve thruster performance. Five models that approximate several of these configurations, along with a sketch of the mesh structure used for calculations, are shown in figure 8. The radial flux distribution was of primary interest in these studies so that a coarse  $x$ -count mesh was used. In addition to the distributor, a "screen-grid" was located across the downstream end of the models. To preserve axial symmetry, the screen-grid was approximated as a series of concentric annuli. The reflection and re-reflection of rays was accomplished as previously discussed. Re-reflected rays are those that strike a downstream surface and return in a negative  $x$ -direction. Because of these rays, two modifications to the computer program were required to prevent the computer from continuously looping. In the first modification, rays that returned to the "orifice" by re-reflection were deleted. In the other modi-

fication, rays that became "trapped" by re-reflection were deleted after 200 re-reflections in the region between the rear wall and the distributor and after 10 re-reflections in the region between the distributor and the screen. These limiting values were selected after considerable investigation of trial solutions run to much higher limits. Both of these "deletion" procedures may be justified to the extent that, under steady-state conditions, the particles, represented by the rays, must eventually find their way out of the chamber, otherwise, chamber pressures would become infinite. The number of deletions resulting from these modifications was actually a small percent of the total number of 720 rays followed. In the worst case, model E, 40 rays (5.6 percent of the total) were deleted. Of these, only four were deleted in the region between the distributor and the screen. This region is of particular interest because the ionization process in the real thruster takes place therein. The weighted value of the deleted rays, however, must be considered to evaluate the effect of these deletions properly. A summation across the screen openings shows that, in the worst case (model E), a total weighted value of less than 4 percent was being deleted.

Flux distributions at four axial stations for the five models studied are plotted in figure 9. Shown in figure 10 are the average flux distributions (two values per opening) through the screen apertures. The curves of figure 9 have the same general form as those of figure 6(a), indicating that the flux distributions are relatively insensitive to distributor geometry. In this respect, the specular-reflection results are in agreement with thruster test results reported in reference 11. Therein, only slight differences in performance were noted in comparing test results from configurations similar to models D and E. As can be seen from figure 8, these two models represent opposite concepts of propellant introduction.

#### CONCLUDING REMARKS

The purpose of this report was to determine particle flux patterns that arise in connection with Knudsen flow in certain geometric configurations of interest in the field of electrostatic propulsion. A basic model of circular cross section was established in which particles were assumed to enter one end through a small orifice and leave the other end, which was wholly open. Two modes of surface reflection were studied: diffuse and specular. Numerical means were used to obtain solutions. The specular-reflection analysis was extended to more complex models that included a distributor and a screen. These models closely approximated variations of a Lewis Research Center electron-bombardment ion thruster. Although the diffuse-reflection analysis could in principle be extended to these models, the additional integral equations that arise make practical solution of the problem extremely difficult.

It was found that, with diffuse reflection, the shape of the flux-distribution curve across the open end of the model approached that of the distribution curve for an infinite tube as the tube length to radius ratio increased. For the model studied, the relative flux distribution along the side wall was found to be linear in part and fitted a rule-of-thumb relation. Differences in flux values at surface intersections were found and were postulated to be due to differing "view factors."



Flux-distribution curves for both the specular- and diffuse-reflection analyses showed maximum values on the axis and minimum values at the wall: between, the distribution curves had opposite curvatures. Increasing the length of the model as well as inclusion of distributors with various openings had little effect on the specular-reflection flux distributions. This insensitivity to distributor geometry has also been noted in measured performance of electron-bombardment thrusters. Since diffuse reflection is generally agreed to be more likely than specular reflection, it must follow that flux distributions obtained from the diffuse-reflection analysis should be closer to the actual case.

Lewis Research Center

National Aeronautics and Space Administration

Cleveland, Ohio, September 24, 1963

## APPENDIX A

### SYMBOLS

A	area, surface
d	diameter of orifice
F	function in eq. (6), defined in appendix B
f	distance, variable, used in derivations in appendix B
G	function in eq. (7), defined in appendix B
g	distance, variable, used in derivations in appendix B
H,I	functions in eq. (7), defined in appendix B
J,K	functions in eq. (8), defined in appendix B
L	length of model
l	length, variable
M	function in eq. (8), defined in appendix B
m	distance, variable, used in derivations in appendix B
N	normal to surface
n	density, particles per unit volume
$\bar{n}$	flow rate, particles per unit time
$\dot{n}$	flux, particles per unit time per unit area
R	radius of model
r	radial distance, variable
S	area, differential
s	radial distance, variable, plane of open end of model
$\bar{v}$	mean particle speed, distance per unit time
x	distance, variable
$\alpha$	number, 1,2,3, . . . , $\infty$
$\beta$	angle, variable, used in derivations in appendix B

$\theta$  angle, variable, between  $N$  and  $l$ , measured from  $N$   
 $\varphi$  angle, variable  
 $\omega$  solid angle

Subscripts:

$b$  band on hemisphere  
 $h$  hemisphere  
 $i, j$  number  
 $p$  plane, normal to x-axis  
 $1$  orifice  
 $2$  open end  
 $3$  side wall  
 $4$  rear wall

## APPENDIX B

### DERIVATION OF INTEGRAL EQUATIONS USED IN

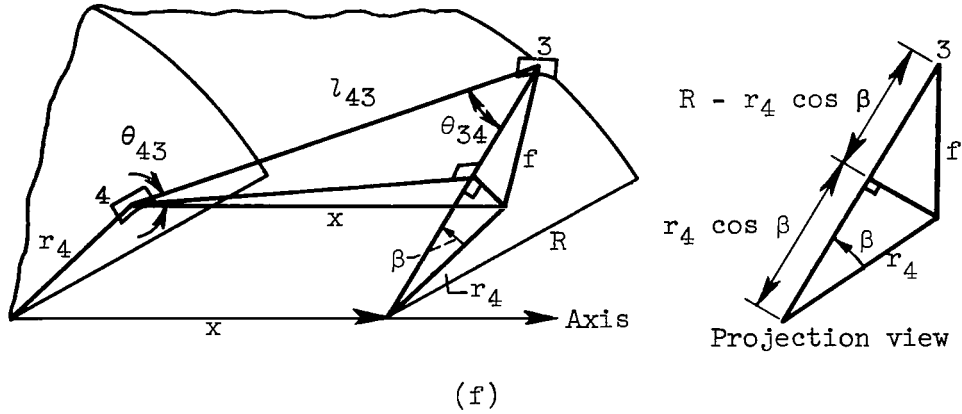
#### DIFFUSE-REFLECTION ANALYSIS

Equations (6) to (8) are established by considering the contributions to the local flux on a surface from all possible sources and then by integrating over the contributing surfaces (i.e., by application of eq. (4)). Subscript numbering in the following derivations and sketches is consistent with that on the model shown in figure 2.

#### I. Equation (6) derivation.

The contribution to the local flux on the rear wall at a point  $r_4$  from a local point on the side wall (see sketch (f)) is

$$d\dot{n}_4(r_4) = \frac{\dot{n}_3}{\pi} \cos \theta_{43} \cos \theta_{34} \frac{dS_3}{l_{43}^2} \quad (B1)$$



The following relations are established from sketch (f):

$$dS_3 = R \, d\beta \, dx. \quad \cos \theta_{43} = \frac{x}{l_{43}}$$

$$\cos \theta_{34} = \frac{R - r_4 \cos \beta}{l_{43}} \quad f^2 = l_{43}^2 - x^2$$

Using these relations in equation (B1) yields

$$d\dot{n}_4(r_4) = \frac{\dot{n}_3\left(\frac{x}{l_{43}}\right)}{\pi} \left( \frac{R - r_4 \cos \beta}{l_{43}} \right) \frac{R}{l_{43}^2} d\beta dx \quad (B2)$$

Also, from the law of cosines,

$$\cos \beta = \frac{R^2 + r_4^2 - l_{43}^2}{2Rr_4} = \frac{R^2 + r_4^2 + x^2 - l_{43}^2}{2Rr_4}$$

from which

$$l_{43}^2 = R^2 + r_4^2 + x^2 - 2Rr_4 \cos \beta$$

The integral over all of the side wall yields the total local flux at a point on the rear wall:

$$\dot{n}_4(r_4) = \frac{2}{\pi} \int_0^L \dot{n}_3(x) R x \int_0^\pi \frac{R - r_4 \cos \beta}{(R^2 + r_4^2 + x^2 - 2Rr_4 \cos \beta)^2} d\beta dx \quad (B3)$$

The flux distribution on the side wall is independent of  $\beta$ , and the  $\beta$  integration can be performed (ref. 12) to obtain equation (6):

$$\dot{n}_4(r_4) = \int_0^L \dot{n}_3(x) F(x, r_4) dx \quad (6)$$

where

$$F(x, r_4) = 2R^2 \frac{x^3 + (R^2 - r_4^2)x}{\left[ x^4 + 2(R^2 + r_4^2)x^2 + (R^2 - r_4^2)^2 \right]^{3/2}} \quad (B4)$$

A condition on the  $\beta$  integration given is that

$$(R^2 + r_4^2 + x^2)^2 > (-2Rr_4)^2$$

This condition is everywhere satisfied except at the point  $x = 0, r_4 = R$ .

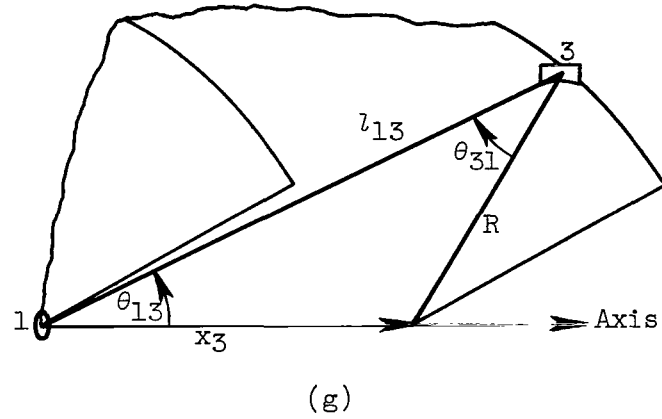
## II. Equation (7) derivation.

The contributions to the local flux on the side wall at a point  $x_3$  come

from three sources: the orifice, the rear wall, and the side wall itself. The equation will be developed by considering each of these in order, with notation as shown in the sketches.

A. The contribution from the orifice, considered as a point source, (see sketch (g)) is

$${}_1\dot{n}_3(x_3) = \frac{\dot{n}_1}{\pi} \cos \theta_{31} \cos \theta_{13} \frac{dS_1}{l_{13}^2} \quad (B5)$$



The following relations are established from sketch (g):

$$\int_A dS_1 = \frac{\pi}{4} d_1^2 \quad \cos \theta_{13} = \frac{x_3}{l_{13}}$$

$$\cos \theta_{31} = \frac{R}{l_{13}} \quad l_{13}^2 = R^2 + x_3^2$$

Using these relations in equation (B5) yields the total contribution from the orifice

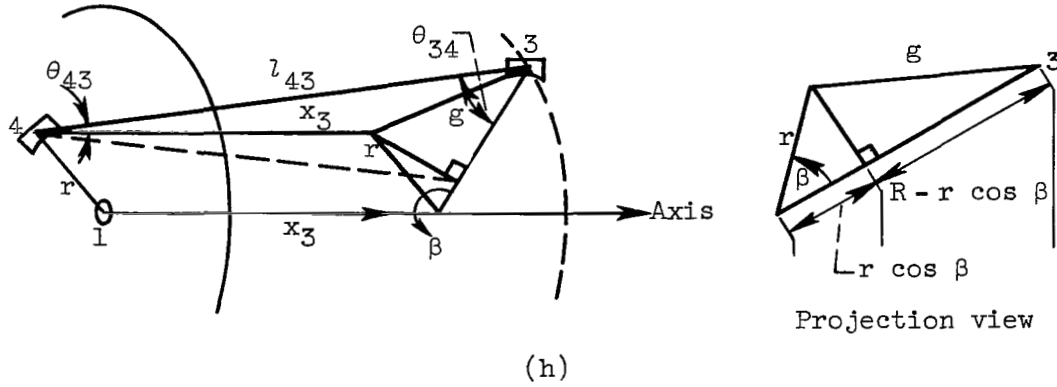
$${}_1\dot{n}_3(x_3) = \dot{n}_1 G(x_3) \quad (B6)$$

where

$$G(x_3) = \frac{x_3 R d_1^2}{4(R^2 + x_3^2)^2} \quad (B7)$$

B. The contribution from a local point on the rear wall (see sketch (h)) is

$$4\dot{n}_3(x_3) = \frac{\dot{n}_4}{\pi} \cos \theta_{34} \cos \theta_{43} \frac{dS_4}{l_{43}^2} \quad (B8)$$



The following relations are established from sketch (h):

$$\begin{aligned} dS_4 &= r \, d\beta \, dr & \cos \theta_{43} &= \frac{x_3}{l_{43}} \\ \cos \theta_{34} &= \frac{R - r \cos \beta}{l_{43}} & g^2 &= l_{43}^2 - x_3^2 \end{aligned}$$

Using these relations in equation (B8) yields

$$4\dot{n}_3(x_3) = \frac{\dot{n}_4}{\pi} \left( \frac{R - r \cos \beta}{l_{43}} \right) \left( \frac{x_3}{l_{43}} \right) r \, d\beta \, dr \quad (B9)$$

Also, from the law of cosines,

$$\cos \beta = \frac{r^2 + R^2 - g^2}{2rR} = \frac{r^2 + R^2 + x_3^2 - l_{43}^2}{2rR}$$

from which

$$l_{43}^2 = r^2 + R^2 + x_3^2 - 2rR \cos \beta$$

The integral over the rear wall yields that contribution to the total flux at a local point  $x_3$  on the side wall:

$$4\dot{n}_3(x_3) = \frac{2}{\pi} \int_{d_1/2}^R \dot{n}_4(r) x_3 r \int_0^\pi \frac{R - r \cos \beta}{(r^2 + R^2 + x_3^2 - 2rR \cos \beta)^2} d\beta \, dr \quad (B10)$$

The  $\beta$  integration can be performed via reference 12 to yield

$${}_4\dot{n}_3(x_3) = \int_{d_1/2}^R \dot{n}_4(r)H(r, x_3)dr \quad (B11)$$

where

$$H(r, x_3) = 2Rx_3 \frac{(R^2 + x_3^2)r - r^3}{\left[ r^4 + 2(x_3^2 - R^2)r^2 + (R^2 + x_3^2)^2 \right]^{3/2}} \quad (B12)$$

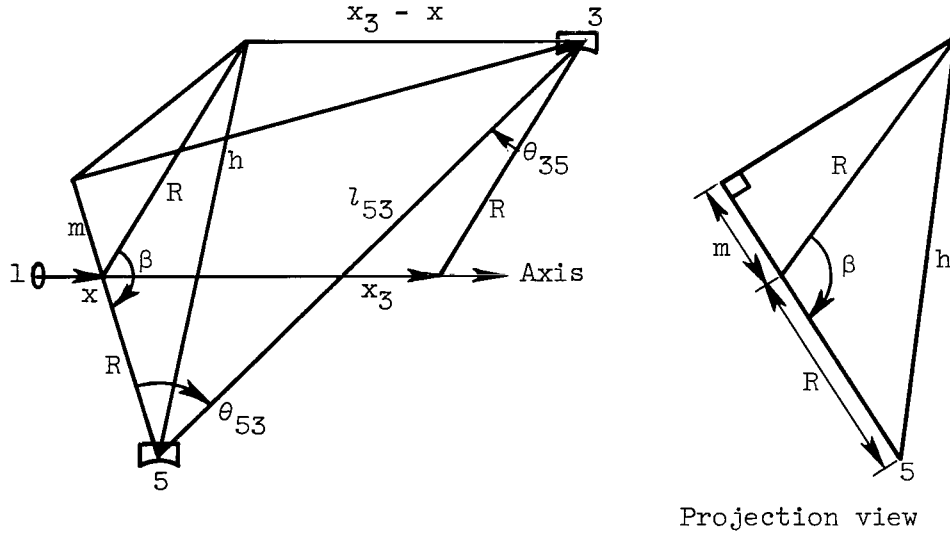
A condition on the  $\beta$  integration in this case is that

$$(r^2 + R^2 + x_3^2)^2 > (-2Rr)^2$$

The condition is satisfied everywhere except at the point  $x_3 = 0, r = R$ .

C. The contribution from a local point (identified as point 5 in sketch (i)) on the side wall itself (see sketch (i)) is

$${}_5d\dot{n}_3(x_3) = \frac{\dot{n}_5}{\pi} \cos \theta_{35} \cos \theta_{53} \frac{dS_5}{l_{53}^2} \quad (B13)$$



(i)

The following relations are established from sketch (i):



$$dS_5 = R \, d\beta \, dx \quad \cos \theta_{35} = \cos \theta_{53} = \frac{R + m}{l_{53}}$$

$$h^2 = l_{53}^2 - (x_3 - x)^2 \quad m = -R \cos \beta$$

Using these relations in equation (B13), and noting that  $\dot{n}_5(x) = \dot{n}_3(x)$ , yields

$$5\dot{n}_3(x_3) = \frac{\dot{n}_3}{\pi} \frac{R^2(1 - \cos \beta)^2}{l_{53}^2} \frac{R \, d\beta \, dx}{l_{53}^2} \quad (B14)$$

From the law of cosines

$$\cos \beta = \frac{R^2 + R^2 - h^2}{2RR}$$

from which

$$h^2 = 2R^2(1 - \cos \beta) = l_{53}^2 - (x_3 - x)^2$$

or

$$l_{53}^2 = 2R^2(1 - \cos \beta) + (x_3 - x)^2$$

The integral over the side wall yields that contribution to the total local flux at a point  $x_3$  on the side wall:

$$5\dot{n}_3(x_3) = \frac{2}{\pi} \int_0^L \dot{n}_3(4)R^3 \int_0^\pi \frac{(1 - \cos \beta)^2}{\left[(x_3 - x)^2 + 2R^2(1 - \cos \beta)\right]^2} d\beta \, dx \quad (B15)$$

After some manipulation, the  $\beta$  integration can be performed via reference 12 to yield

$$5\dot{n}_3(x_3) = \int_0^L \dot{n}_3(x) I(x, x_3) dx \quad (B16)$$

where

$$I(x, x_3) = \frac{1}{2R} \left\{ 1 - |x_3 - x| \frac{(x_3 - x)^2 + 6R^2}{\left[(x_3 - x)^2 + 4R^2\right]^{3/2}} \right\} \quad (B17)$$

and where the magnitude sign preserves the positive sense associated with the leg of the triangle in sketch (i) and permits the contribution over the entire surface of the side wall to be written under one integral. A condition on the  $\beta$  integration in this case is that

$$\left[ (x_3 - x)^2 + 2R^2 \right]^2 > (-2R^2)^2$$

This condition is satisfied everywhere except at the point  $x_3 = x$ . At this point, the latter half of the term in brackets in equation (B17) becomes zero. Note, however, that this portion of the bracketed term is always positive and approaches zero as  $x$  approaches  $x_3$ . Finally, combining equations (B6), (B11), and (B16) yields equation (7):

$$\dot{n}_3(x_3) = \dot{n}_1 G(x_3) + \int_{d_1/2}^R \dot{n}_4(r) H(r, x_3) dr + \int_0^L \dot{n}_3(x) I(x, x_3) dx \quad (7)$$

### III. Equation (8) derivation.

The derivation of equation (8) follows the identical procedure given in the two previous derivations. That is, contributions to the local flux at a point  $s_2$  in the plane of the open end are each determined and then integrated to give the total contribution. In this case the contributing sources are: the orifice, the rear wall, and the side wall. These contributions, when set up in integral form, become

$$\begin{aligned} \dot{n}_2(s_2) = & \frac{\dot{n}_1}{4} \left( \frac{L d_1}{L^2 + s_2^2} \right)^2 + \frac{2}{\pi} \int_{d_1/2}^R \dot{n}_4(r) L^2 r \int_0^\pi \frac{1}{(r^2 + s_2^2 + L^2 - 2rs_2 \cos \beta)^2} d\beta dr \\ & + \frac{2}{\pi} \int_0^L \dot{n}_3(x) R(L-x) \int_0^\pi \frac{R - s_2 \cos \beta}{[R^2 + s_2^2 + (L-x)^2 - 2Rs_2 \cos \beta]^2} d\beta dx \end{aligned} \quad (B18)$$

After the  $\beta$  integration, equation (B18) becomes

$$\dot{n}_2(s_2) = \dot{n}_1 J(s_2) + \int_{d_1/2}^R \dot{n}_4(r) K(r, s_2) dr + \int_0^L \dot{n}_3(x) M(x, s_2) dx \quad (8)$$

where

$$J(s_2) = \frac{1}{4} \left( \frac{Ld_1}{L^2 + s_2^2} \right)^2$$

$$K(r, s_2) = 2L^2 \frac{r^3 + (L^2 + s_2^2)r}{\left[ r^4 + 2(L^2 - s_2^2)r^2 + (L^2 + s_2^2)^2 \right]^{3/2}}$$

$$M(x, s_2) = 2R^2 \frac{(L - x)^3 + (R^2 - s_2^2)(L - x)}{\left[ (L - x)^4 + 2(R^2 + s_2^2)(L - x)^2 + (R^2 - s_2^2)^2 \right]^{3/2}}$$

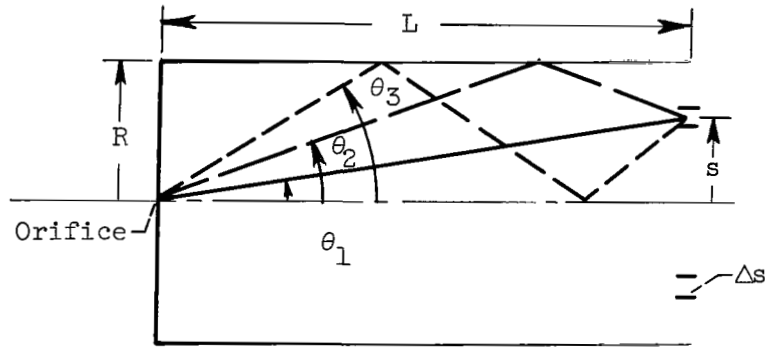
## APPENDIX C

### DERIVATION OF ANALYTIC EXPRESSION FOR SPECULAR-REFLECTION ANALYSIS

In equation (12), an expression for the arrival rate passing through a differential band on a hemisphere is given as

$$d(\bar{n}_b) = \bar{n}_1 2 \cos \theta_1 \sin \theta_1 d\theta_1 \quad (C1)$$

Consider an annulus located at radius  $s$  in a plane transverse to the axis of the basic model, as shown in sketch (j).



(j)

Similar to the method given in the text, particles leaving the orifice in a direction  $\theta_1$  are represented by a ray in the two-dimensional plane. Obviously, an infinite number of rays can pass through the annulus shown in sketch (j). The flux through the annulus is given by the summation of arrival rates of all these rays, divided by the area of the annulus:

$$\dot{n}_2(s_2) = \frac{\bar{n}_1}{2\pi s(\Delta s)} \sum_{i=1}^{\infty} 2 \cos \theta_i \sin \theta_i (\Delta\theta_i) \quad (C2)$$

To establish the series given in equation (C2), consider the three possible paths that rays may take to arrive at the annulus. These are shown typically in sketch (j).

For the first ray  $\theta_1$ ,

$$\cos \theta_1 = \frac{L}{\sqrt{s^2 + L^2}}, \quad \sin \theta_1 = \frac{s}{\sqrt{s^2 + L^2}}$$

$$\Delta\theta_1 = \frac{(\Delta s)\cos \theta_1}{\sqrt{s^2 + L^2}} = \frac{(\Delta s)L}{s^2 + L^2}$$

The next ray  $\theta_2$  first strikes the side wall and is reflected through the annulus. For this ray,

$$\cos \theta_2 = \frac{L}{\sqrt{(2R - s)^2 + L^2}} \quad \sin \theta_2 = \frac{2R - s}{\sqrt{(2R - s)^2 + L^2}}$$

$$\Delta\theta_2 = \frac{(\Delta s)\cos \theta_2}{\sqrt{(2R - s)^2 + L^2}} = \frac{(\Delta s)L}{(2R - s)^2 + L^2}$$

The third ray,  $\theta_3$ , first strikes the side wall and is reflected to the axis. It then re-reflects from the axis and passes through the annulus. For this ray,

$$\cos \theta_3 = \frac{L}{\sqrt{(2R + s)^2 + L^2}} \quad \sin \theta_3 = \frac{2R + s}{\sqrt{(2R + s)^2 + L^2}}$$

$$\Delta\theta_3 = \frac{(\Delta s)\cos \theta_3}{\sqrt{(2R + s)^2 + L^2}} = \frac{(\Delta s)L}{(2R + s)^2 + L^2}$$

Equation (C2) can thus be written as

$$\frac{\dot{n}_2(s)}{\bar{n}_1} = \frac{1}{\pi s(\Delta s)} \left\{ \frac{s(\Delta s)L^2}{(s^2 + L^2)^2} + \frac{(2R - s)(\Delta s)L^2}{[(2R - s)^2 + L^2]^2} + \frac{(2R + s)(\Delta s)L^2}{[(2R + s)^2 + L^2]^2} + \dots \right\} \quad (C3)$$

Equation (C3) reduces to

$$\frac{\dot{n}_2(s)}{\bar{n}_1} = \frac{L^2}{\pi s} \left\{ \sum_{\alpha=0}^{\infty} \frac{2\alpha R + s}{[(2\alpha R + s)^2 + L^2]^2} + \sum_{\alpha=1}^{\infty} \frac{2\alpha R - s}{[(2\alpha R - s)^2 + L^2]^2} \right\} \quad (C4)$$

Normalized with respect to  $R$  and with  $\bar{n}_1 = \dot{n}_1(\pi/4)(d_1/2)^2$ , equation (C4) may be written to express the relative flux ratio:

$$\frac{\dot{n}_2(s)}{\dot{n}_1} = \frac{1}{4} \left(\frac{d_1}{2}\right)^2 \frac{\left(\frac{L}{R}\right)^2}{\frac{s}{R}} \left\{ \sum_{\alpha=0}^{\infty} \frac{2\alpha + \frac{s}{R}}{\left[\left(2\alpha + \frac{s}{R}\right)^2 + \left(\frac{L}{R}\right)^2\right]^2} + \sum_{\alpha=1}^{\infty} \frac{2\alpha - \frac{s}{R}}{\left[\left(2\alpha - \frac{s}{R}\right)^2 + \left(\frac{L}{R}\right)^2\right]^2} \right\} \quad (C5)$$

Inspection of equation (C5) shows that the term by term contributions are of the order of  $1/\alpha^3$ , so that only a few terms are needed for accurate solution.

## REFERENCES

1. Present, R. D.: Kinetic Theory of Gases. McGraw-Hill Book Co., Inc., 1958. (Ch. 1-4.)
2. Dayton, B. B.: Gas Flow Patterns at Entrance and Exits of Cylindrical Tubes. Consolidated Electrodynamics Corp., Sept. 13, 1956.
3. Demarcus, W. C.: The Problem of Knudsen Flow. Rep. K-1302, Pts. I-VI, AEC, 1956-1957.
4. Bureau, A. J., Laslett, L. Jackson, and Keller, J. M.: The Pumping Speed of a Circular Aperture in a Diaphragm Across a Circular Tube. Rev. Sci. Instr., vol. 23, no. 12, Dec. 1952, pp. 683-686.
5. Sparrow, E. M., Jonsson, V. K., and Lundgren, T. S.: Free-Molecule Tube Flow and Adiabatic Wall Temperatures. Jour. Heat Transfer (Trans. ASME), ser. C, vol. 85, no. 2, May 1963, pp. 111-118.
6. Sparrow, E. M., and Jonsson, V. K.: Free-Molecule Flow and Convective-Radiative Energy Transport in a Tapered Tube or Conical Nozzle. AIAA Jour., vol. 1, no. 5, May 1963, pp. 1081-1087.
7. Kaufman, Harold R.: An Ion Rocket with an Electron-Bombardment Ion Source. NASA TN D-585, 1961.
8. Toomre, Alar: Gas Dynamics of Free Molecule Flow. TN 58-787, Office Sci. Res., Mar. 1958.
9. Bird, G. A.: The Distribution of Reflected Molecules from Typical Bodies in Rarefied Gas Flow. Tech. Note HSA 56, Weapons Res. Establishment, (Australia), Jan. 1960.
10. Sparrow, E. M., Albers, L. U., and Eckert, E. R. G.: Thermal Radiation Characteristics of Cylindrical Enclosures. Jour. Heat Transfer (Trans. ASME), ser. C, vol. 84, no. 1, Feb. 1962, pp. 73-81.
11. Kaufman, H. R., and Reader, P. D.: Experimental Performance of an Ion Rocket Employing an Electron Bombardment Ion Source. Preprint 1374-60, Am. Rocket Soc., Inc., 1960.
12. Dwight, Herbert Bristol: Tables of Integrals and Other Mathematical Data. Fourth ed., The Macmillan Co., 1961, pp. 105-106.

TABLE I. - VALUES OF RATIO TEST  
AND NUMBER OF ITERATIONS  
OF EQUATIONS (6) AND (7)

Length to radius ratio, L/R	Ratio <sup>a</sup>	Number of iterations
1	0.992	20
2	.987	20
3	.981	20
4	.977	80
5	.971	60
10	.968	20

<sup>a</sup>The ratio is defined as follows:

$$\text{Ratio} = \frac{\int_0^R [\dot{n}_2(s)/\dot{n}_1] s \, ds}{1/2(d_1/2)^2}$$

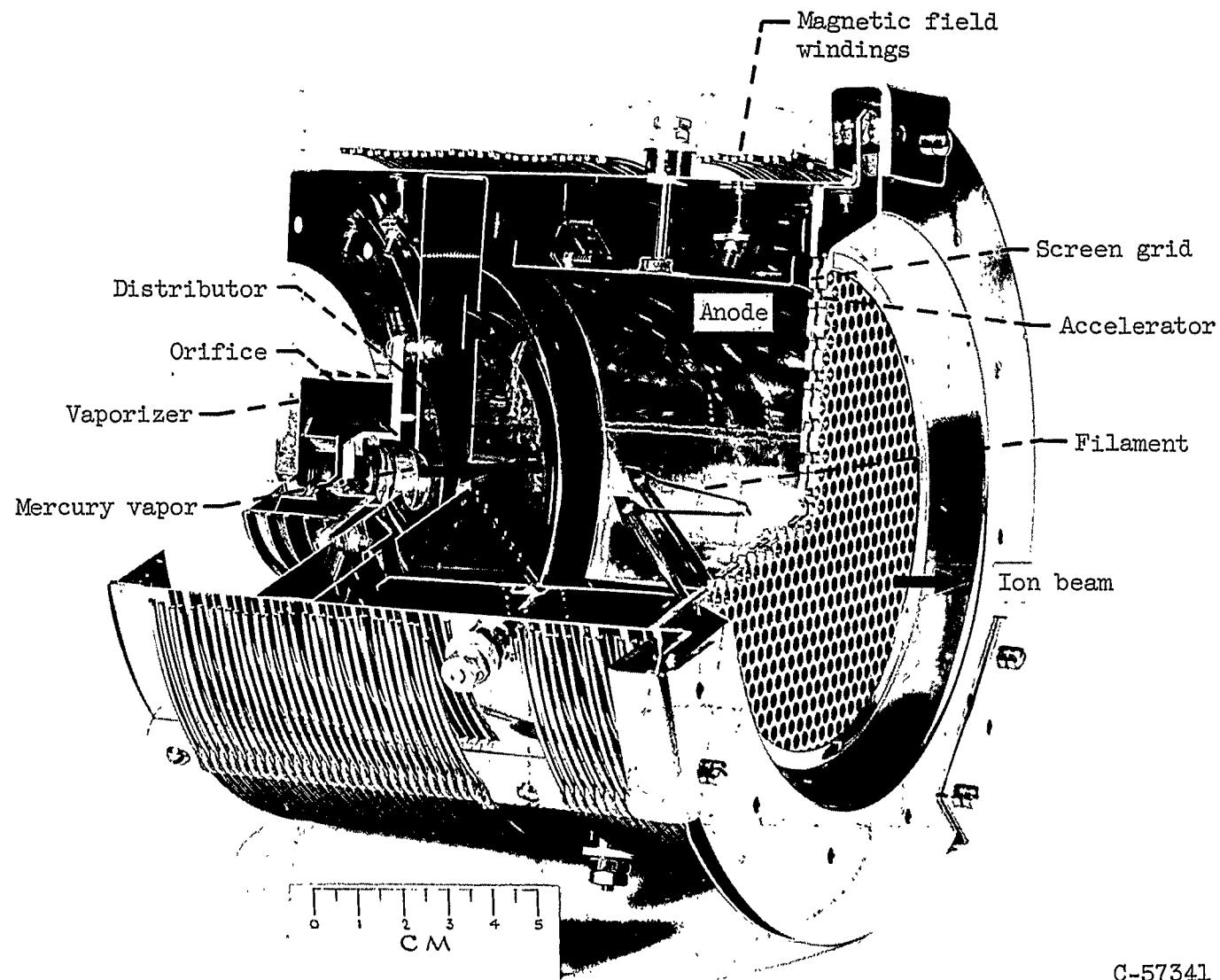
TABLE II. - END-POINT VALUES OF RELATIVE FLUX DISTRIBUTION  
CURVES OF FIGURES 3 to 5 FOR DIFFUSE-REFLECTION  
ANALYSIS OF MODEL SHOWN IN FIGURE 2

Length to radius ratio, L/R	Rear wall, $\dot{n}_4(r)/\dot{n}_1$ (fig. 3)		Side wall, $\dot{n}_3(x)/\dot{n}_1$ (fig. 5)		Open end, $\dot{n}_2(s)/\dot{n}_1$ (fig. 4)	
	Position		Position		Position	
	Radial, r/R		Axial, x/R		Radial, s/R	
	$d_1/2R$	$1^a$	$0^a$	$(L/R)^b$	$1^b$	$0$
1	$0.069 \times 10^{-2}$	$0.029 \times 10^{-2}$	$0.043 \times 10^{-2}$	$0.114 \times 10^{-2}$	$0.108 \times 10^{-2}$	$0.333 \times 10^{-2}$
2	.178	.076	.098	.108	.131	.254
3	.276	.123	.148	.107	.135	.249
4	.371	.168	.197	.102	.136	.248
5	.461	.213	.242	.101	.136	.246
10	.902	.429	.462	.098	.138	.244

<sup>a</sup>Corresponding points.

<sup>b</sup>Corresponding points.





C-57341

Figure 1. - Electron-bombardment ion thruster.

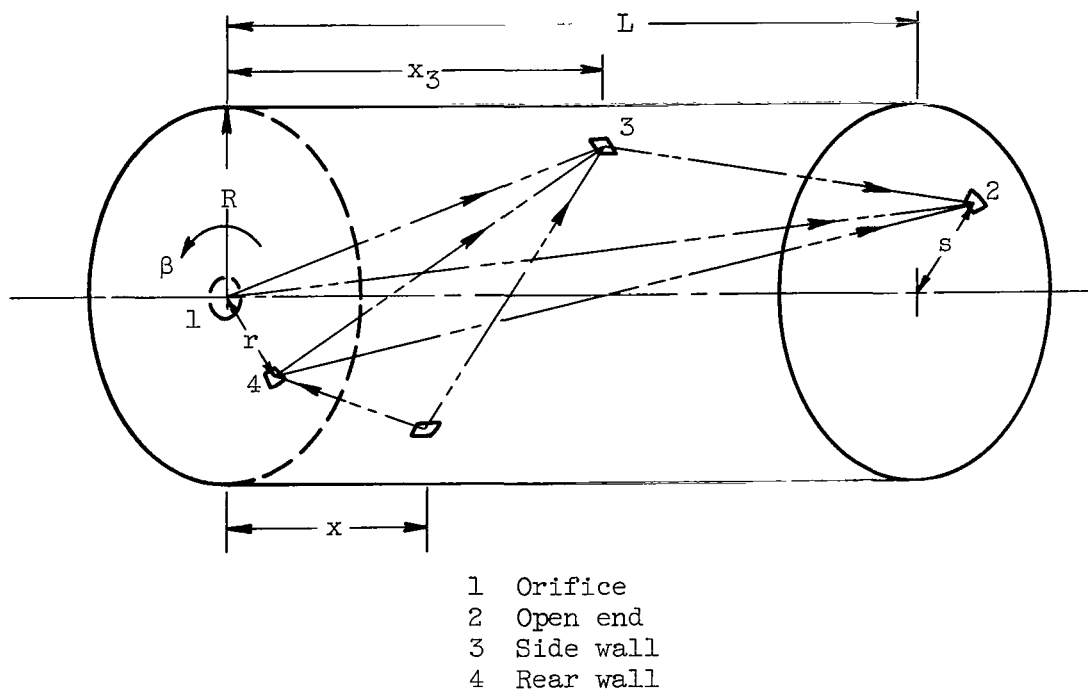


Figure 2. - Basic model for diffuse- and specular-reflection analyses.

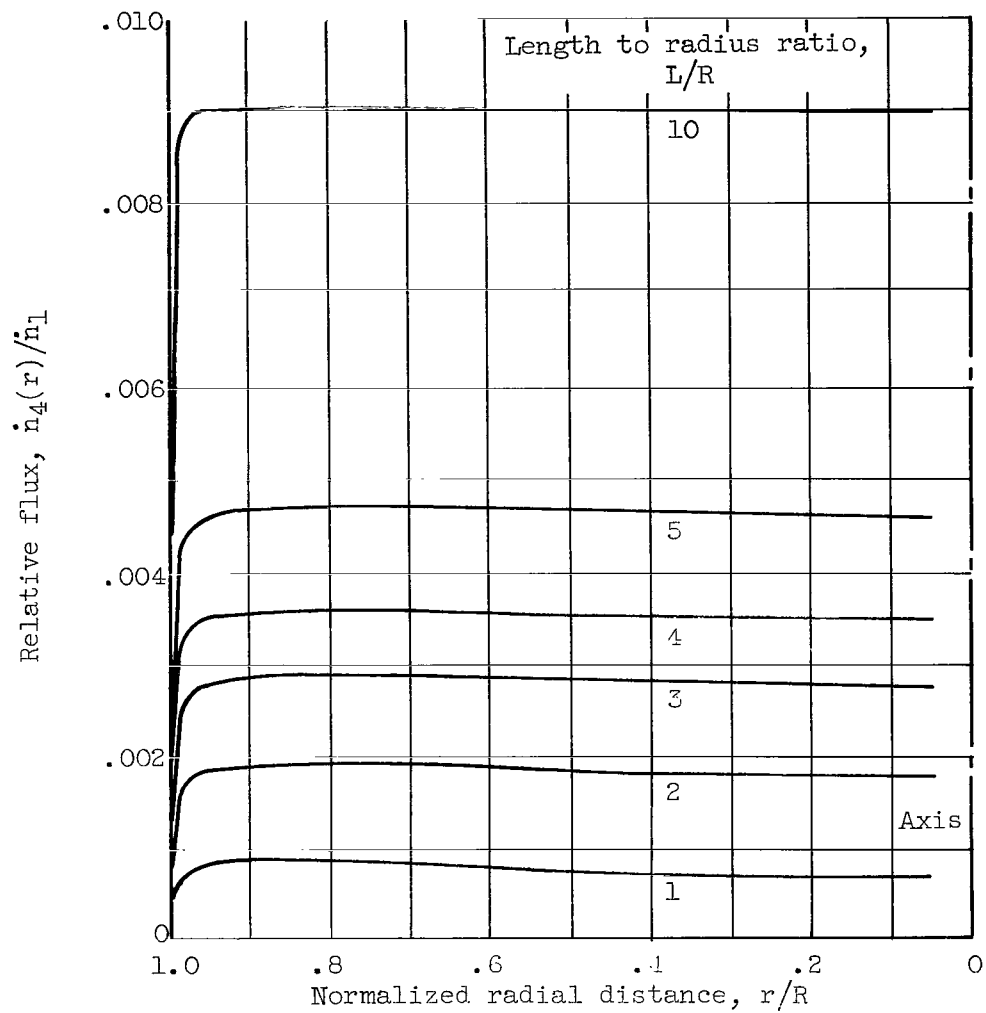


Figure 3. - Relative flux distribution along rear wall of model shown in figure 2 for various length to radius ratios. Diffuse-reflection analysis. Radius of orifice, 0.0476 units.

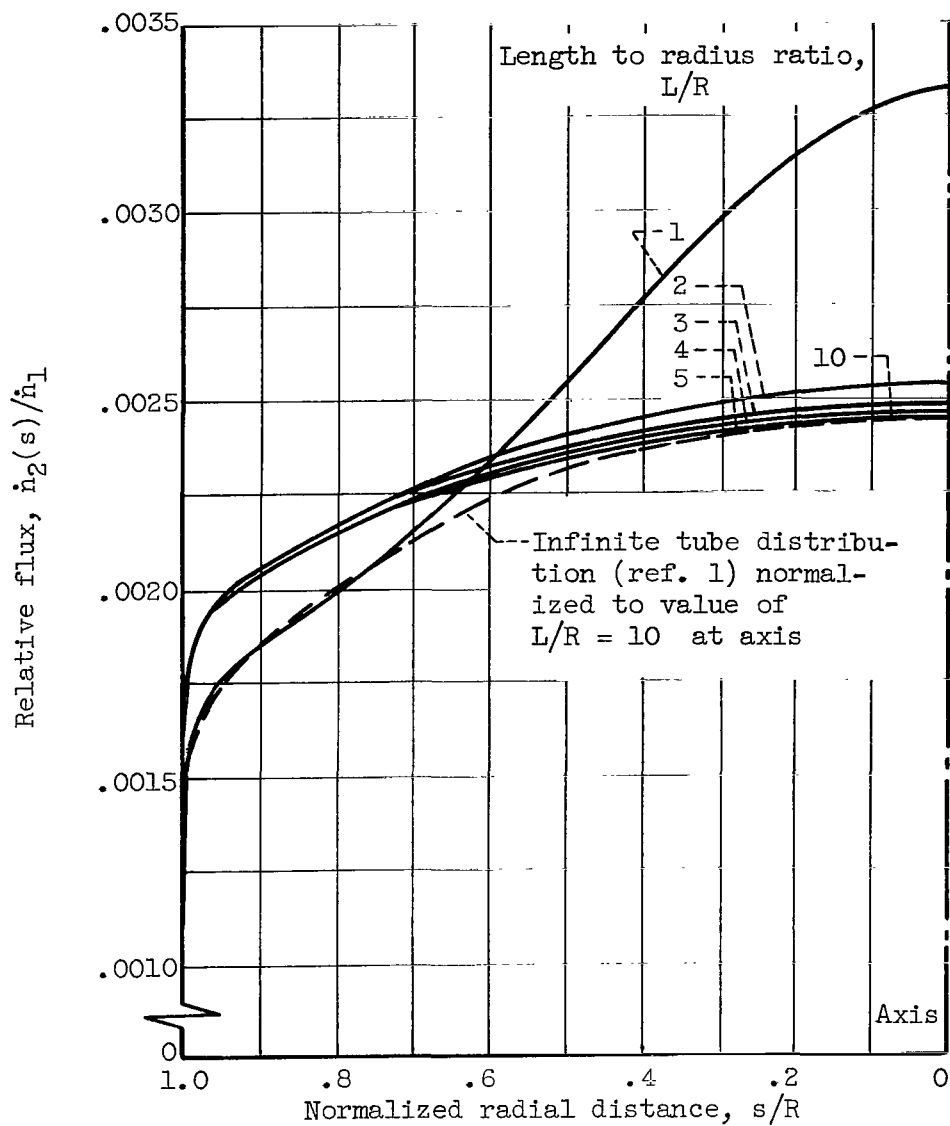


Figure 4. - Relative flux distribution along open end of model shown in figure 2 for various length to radius ratios. Diffuse-reflection analysis. Radius of orifice, 0.0476 units.

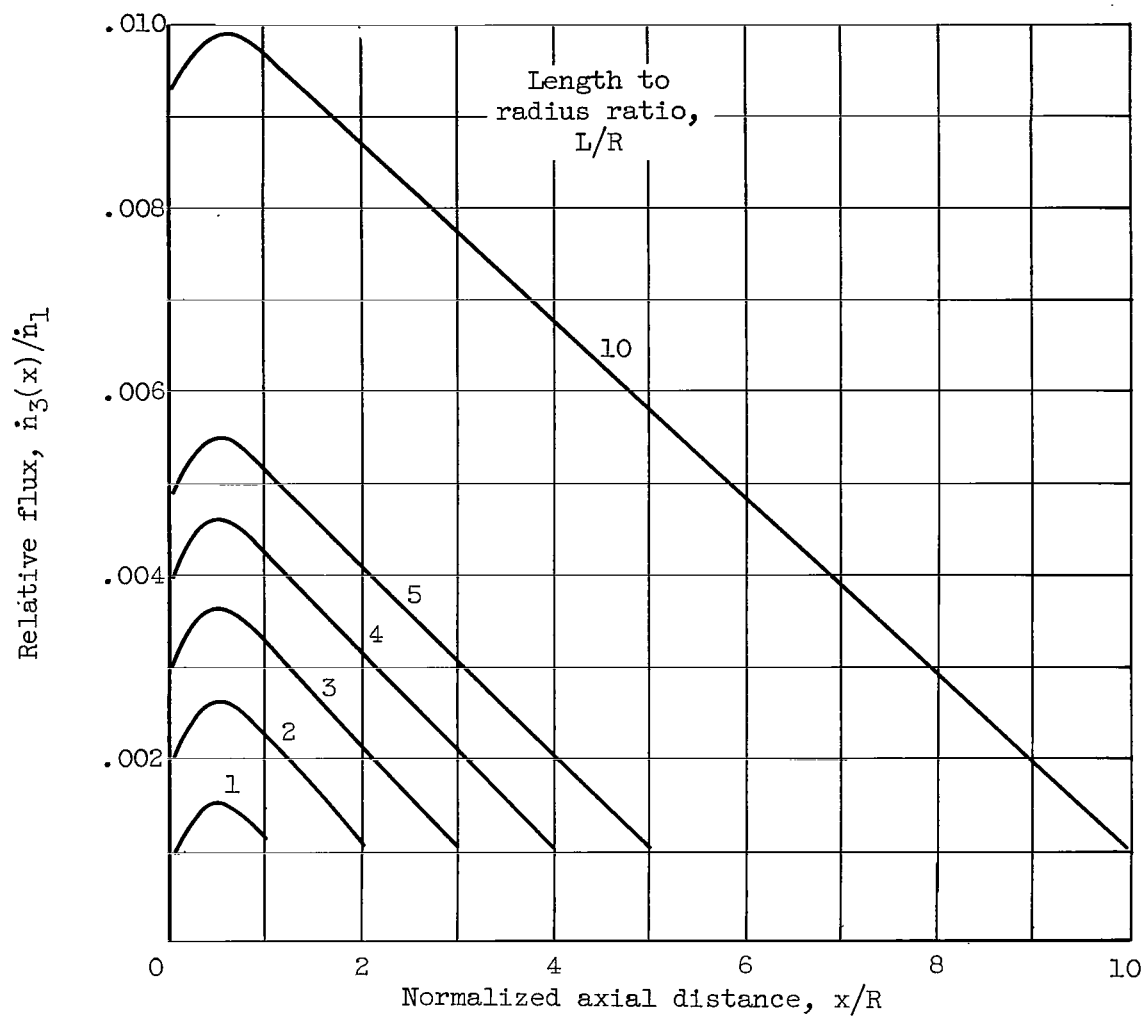
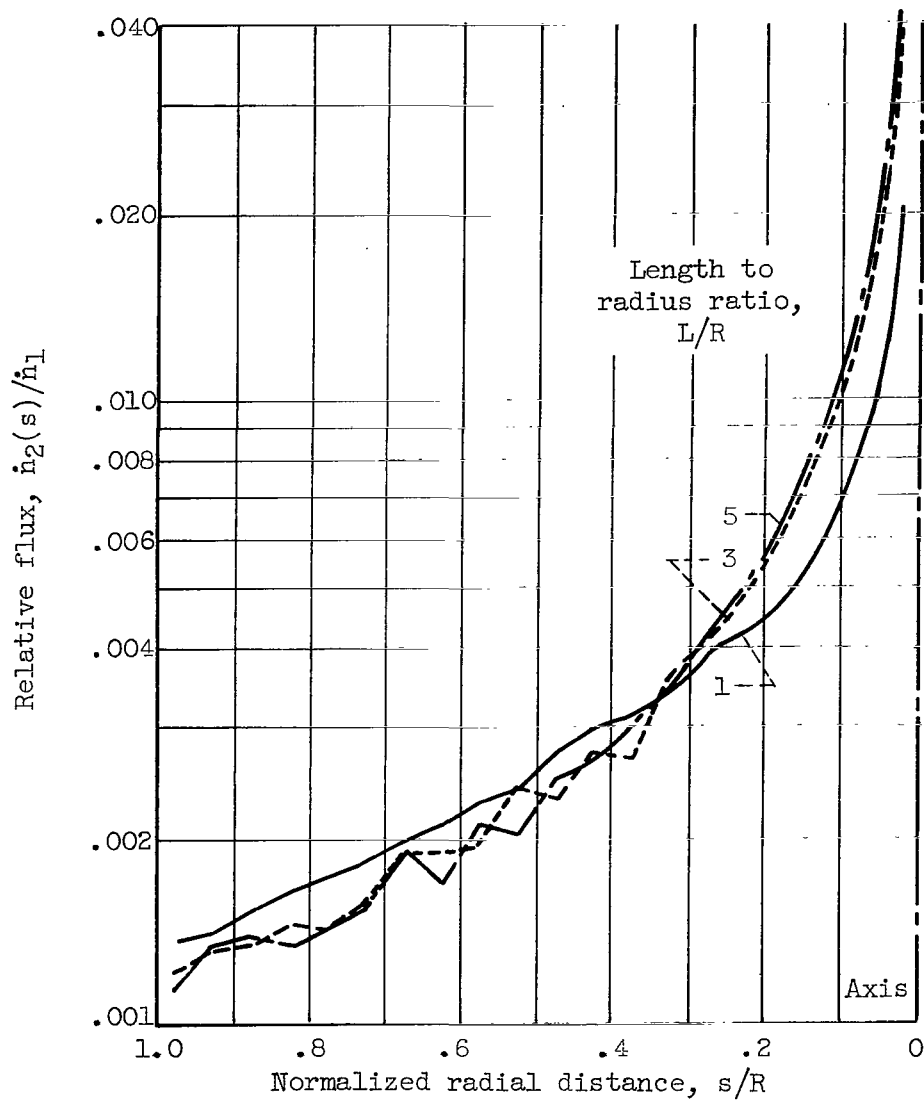
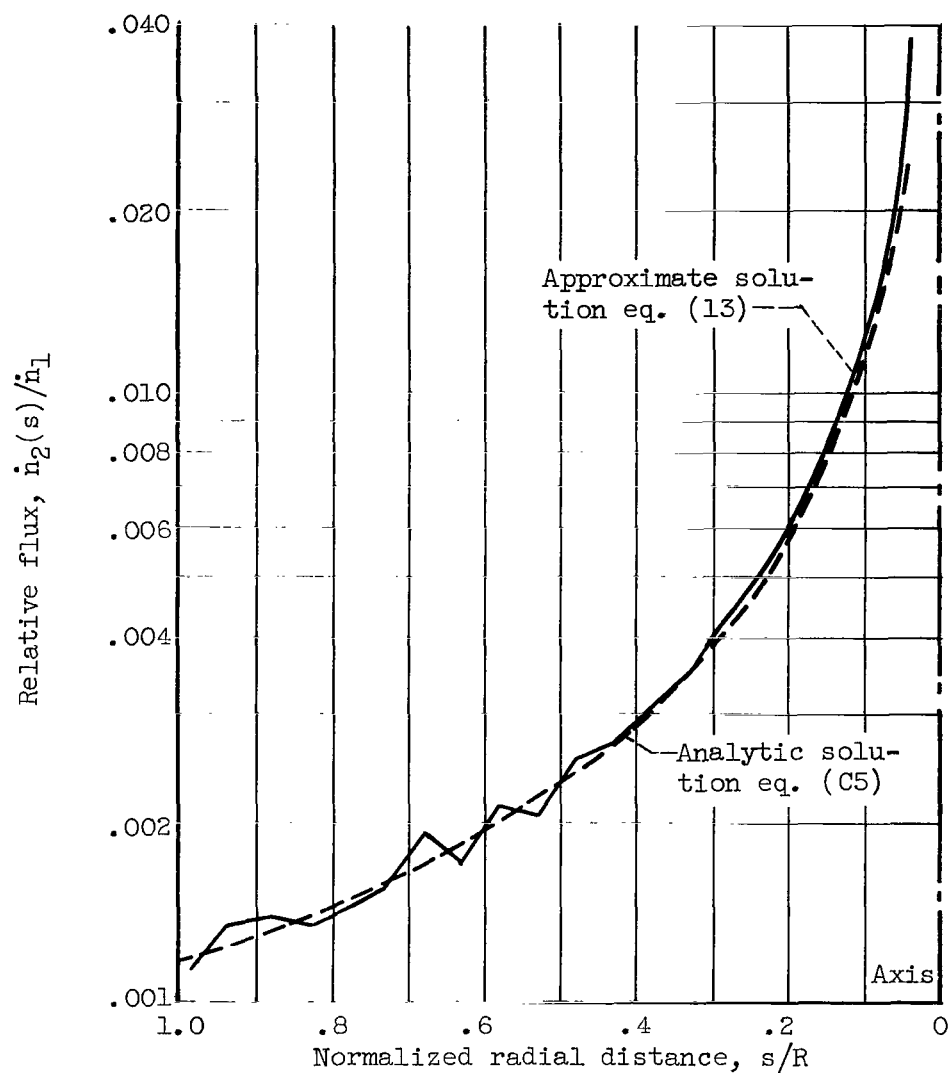


Figure 5. - Relative flux distribution along side wall of model shown in figure 2 for various length to radius ratios. Diffuse-reflection analysis. Radius of orifice, 0.0476 units.



(a) Various length to radius ratios.  
Compare with figure 4.

Figure 6. - Relative flux distribution along  
open end of model shown in figure 2.  
Specular-reflection analysis.



(b) Comparison of approximate and analytic results for a length to radius ratio of 5.

Figure 6. - Concluded. Relative flux distribution along open end of model shown in figure 2. Specular-reflection analysis.

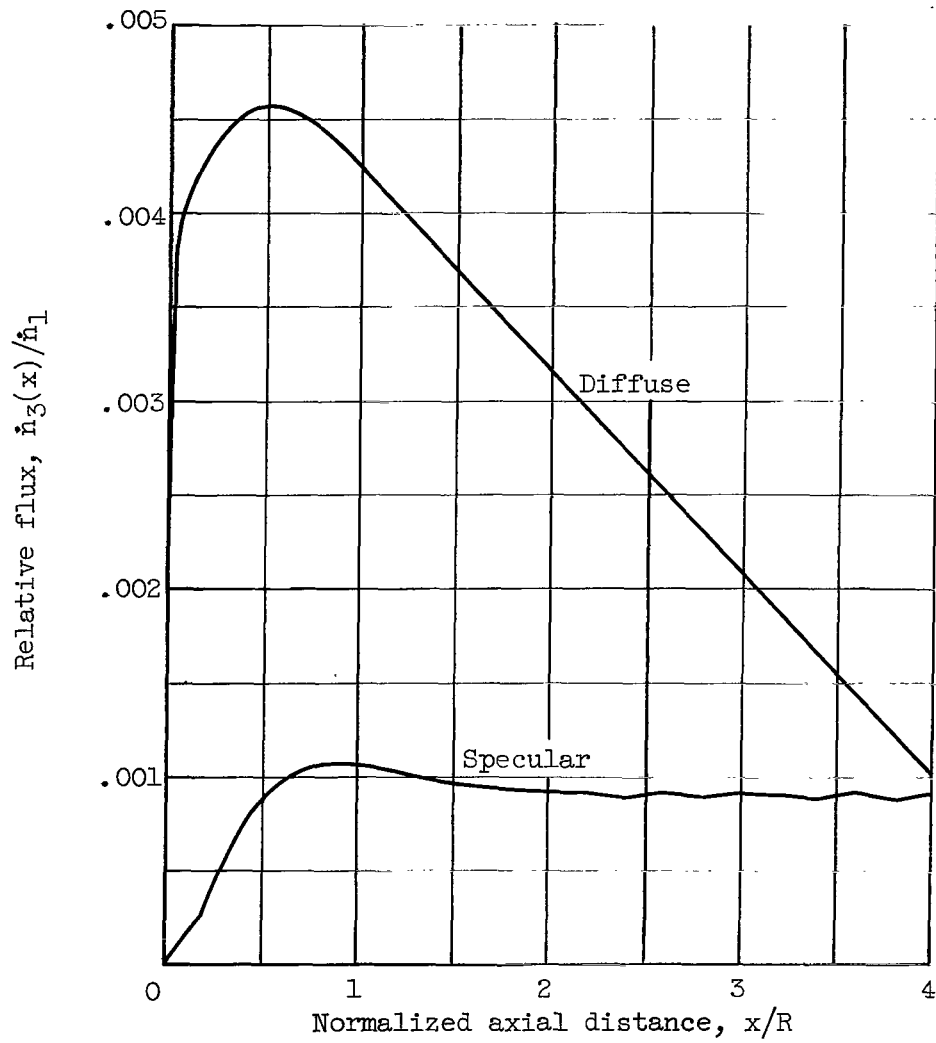
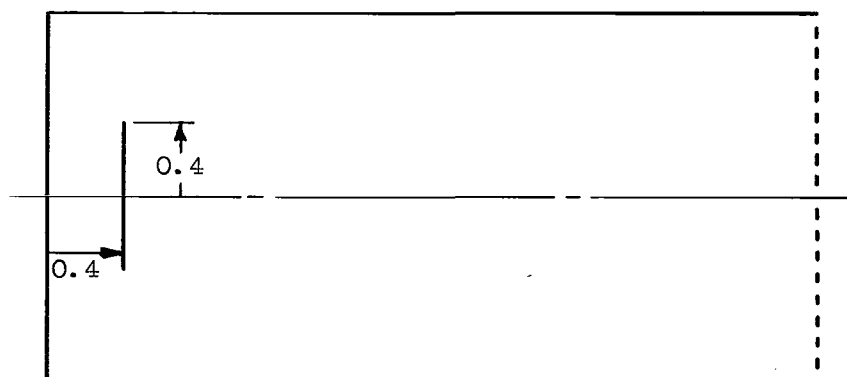
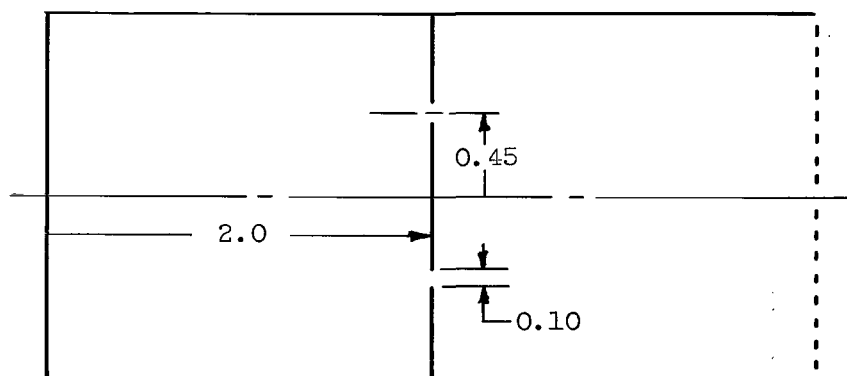


Figure 7. - Comparison of relative flux distribution along side wall of model shown in figure 2. Length to radius ratio, 4. Diffuse- and specular-reflection analysis.

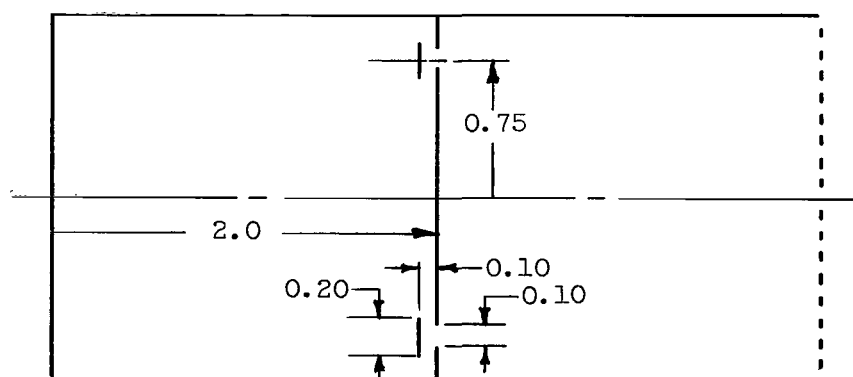




Model A

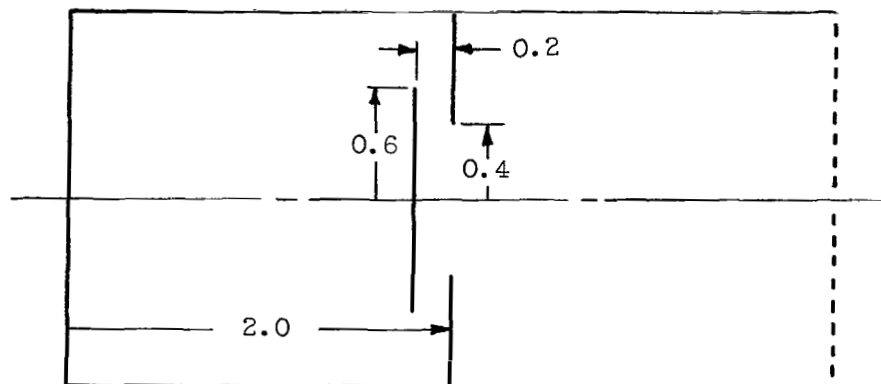


Model B

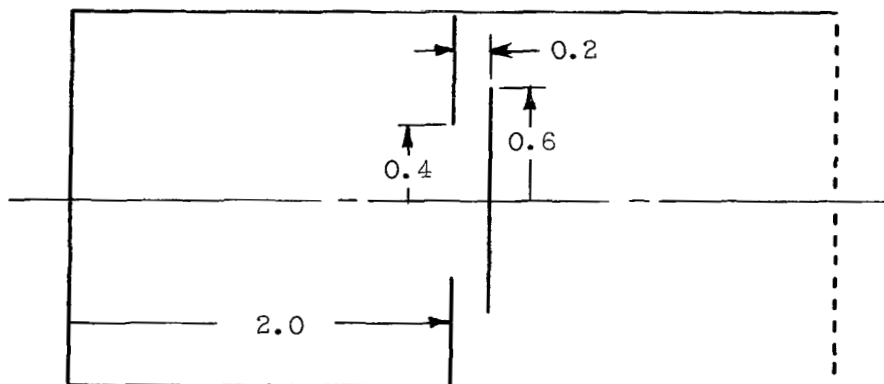


Model C

Figure 8. - Section views of ion-thruster models and mesh overlay for specular reflection analysis. Length, 4; radius, 1. Normalized units. Nine equally spaced concentric screen openings, 0.08 units each.



Model D



Model E

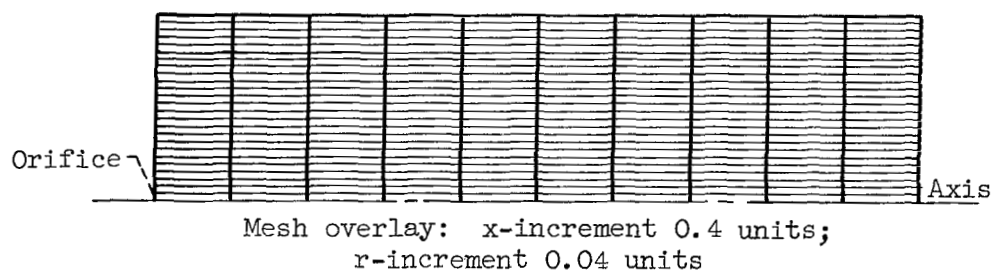
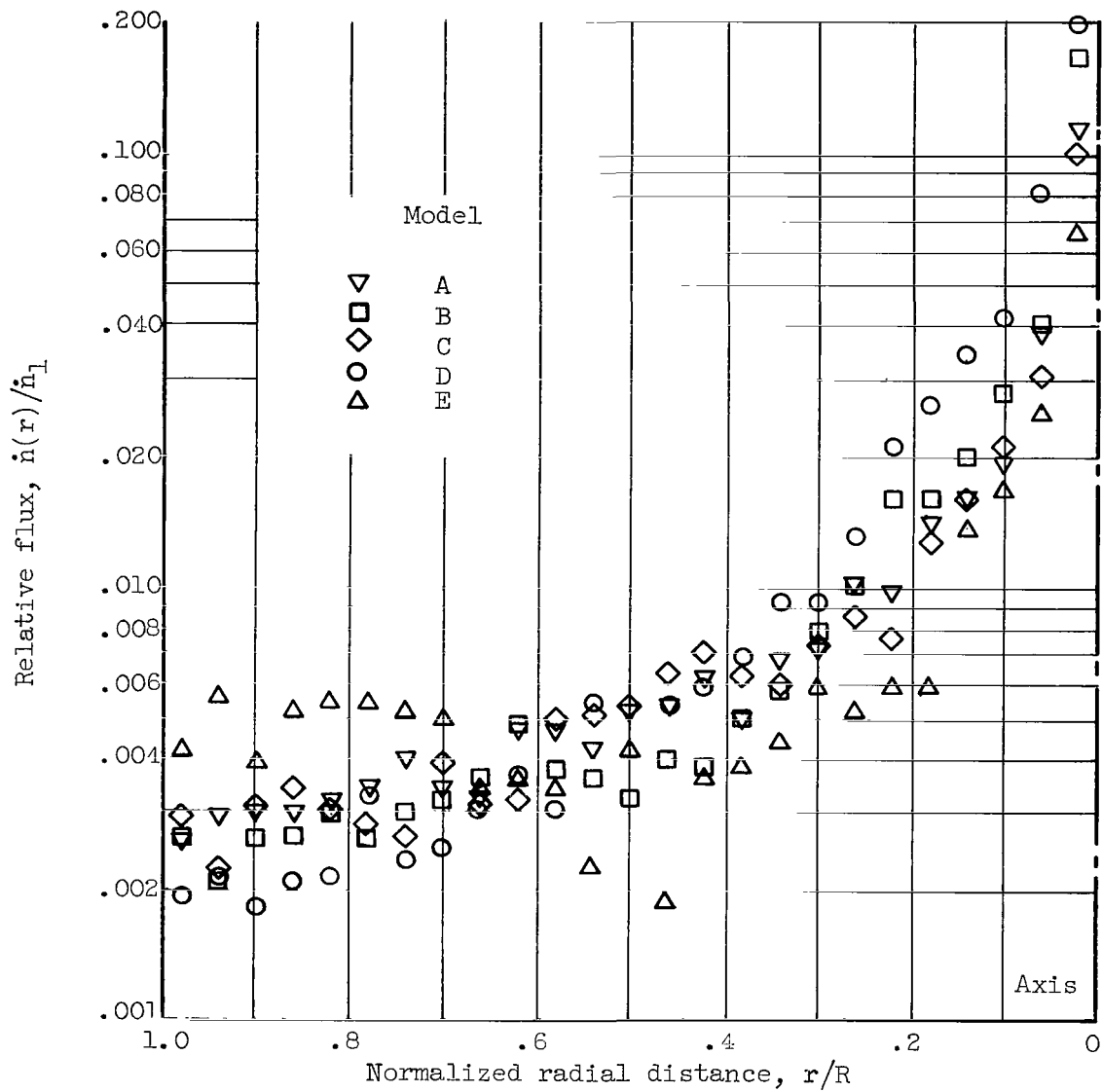
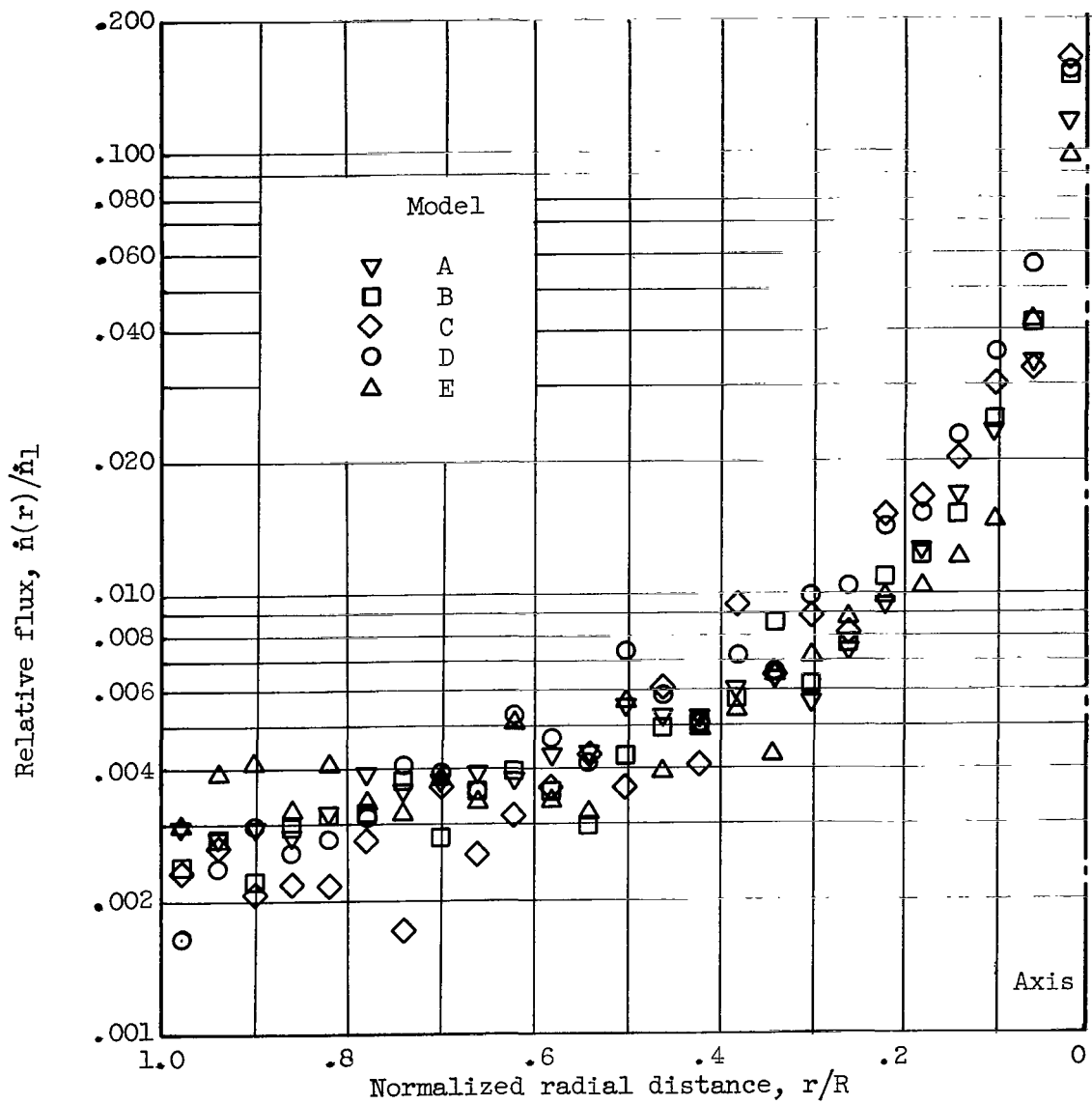


Figure 8. - Concluded. Section views of ion-thruster models and mesh overlay for specular reflection analysis. Length, 4; radius, 1. Normalized units. Nine equally spaced concentric screen openings, 0.08 units each.



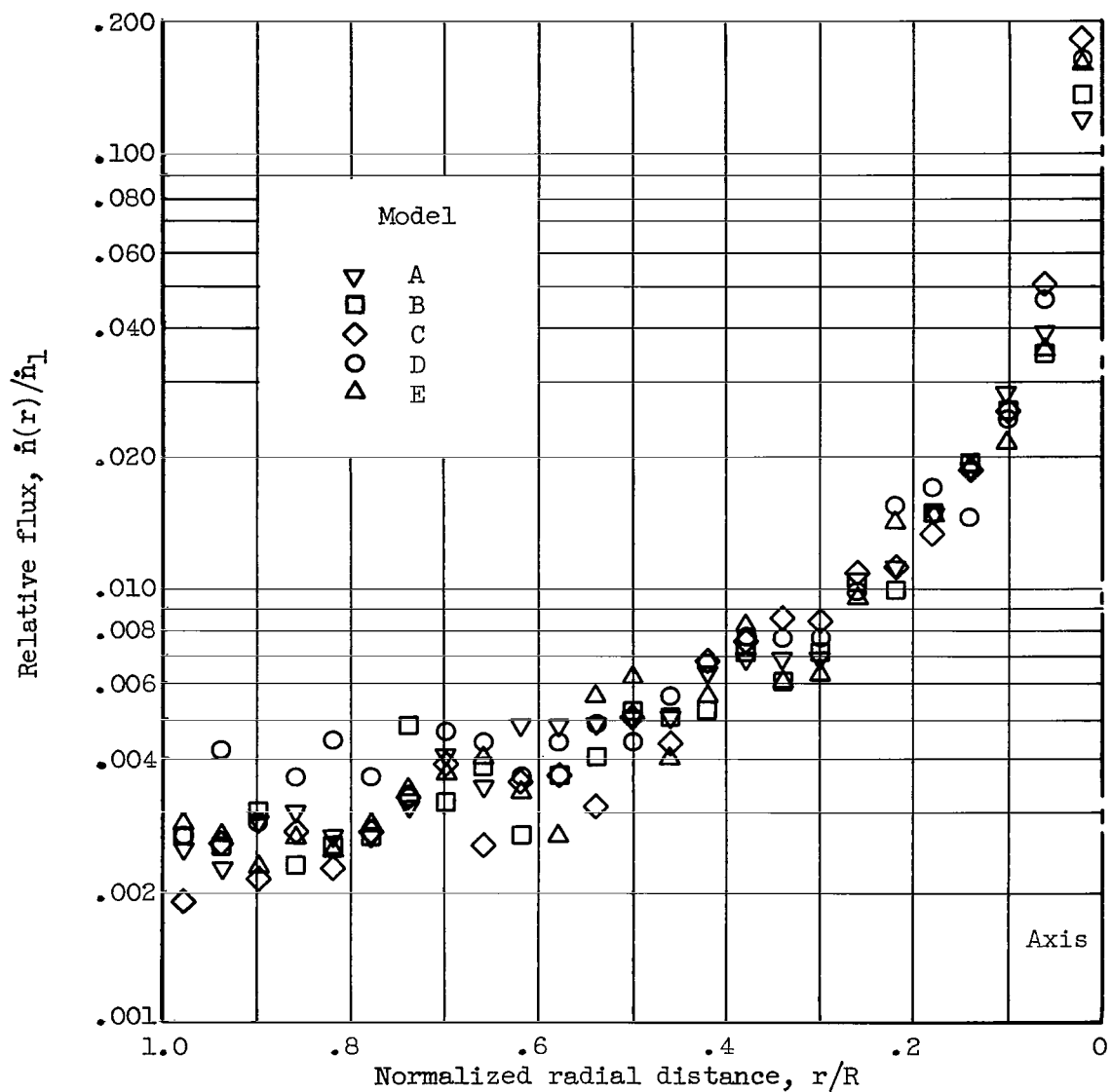
(a) Normalized axial distance from orifice, 2.4 units.

Figure 9. - Specular reflection relative radial flux distribution at various normalized axial distances from orifice for models shown in figure 8.



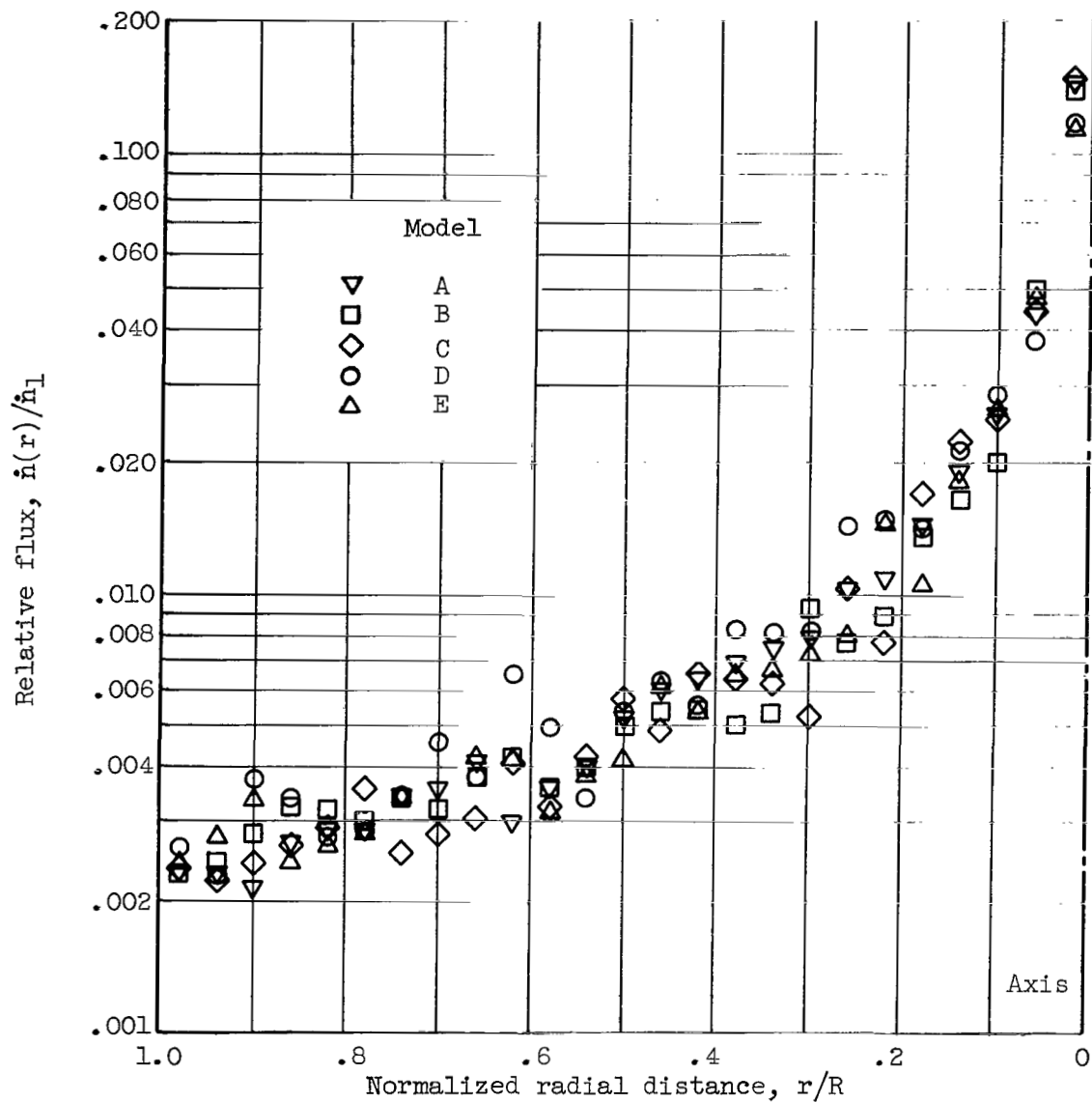
(b) Normalized axial distance from orifice, 2.8 units.

Figure 9. - Continued. Specular reflection relative radial flux distributions at various normalized axial distances from orifice for models shown in figure 8.



(c) Normalized axial distance from orifice, 3.2 units.

Figure 9. - Continued. Specular reflection relative radial flux distributions at various normalized axial distances from orifice for models shown in figure 8.



(d) Normalized axial distance from orifice, 3.6 units.

Figure 9. - Concluded. Specular reflection relative radial flux distributions at various normalized distances from orifice for models shown in figure 8.

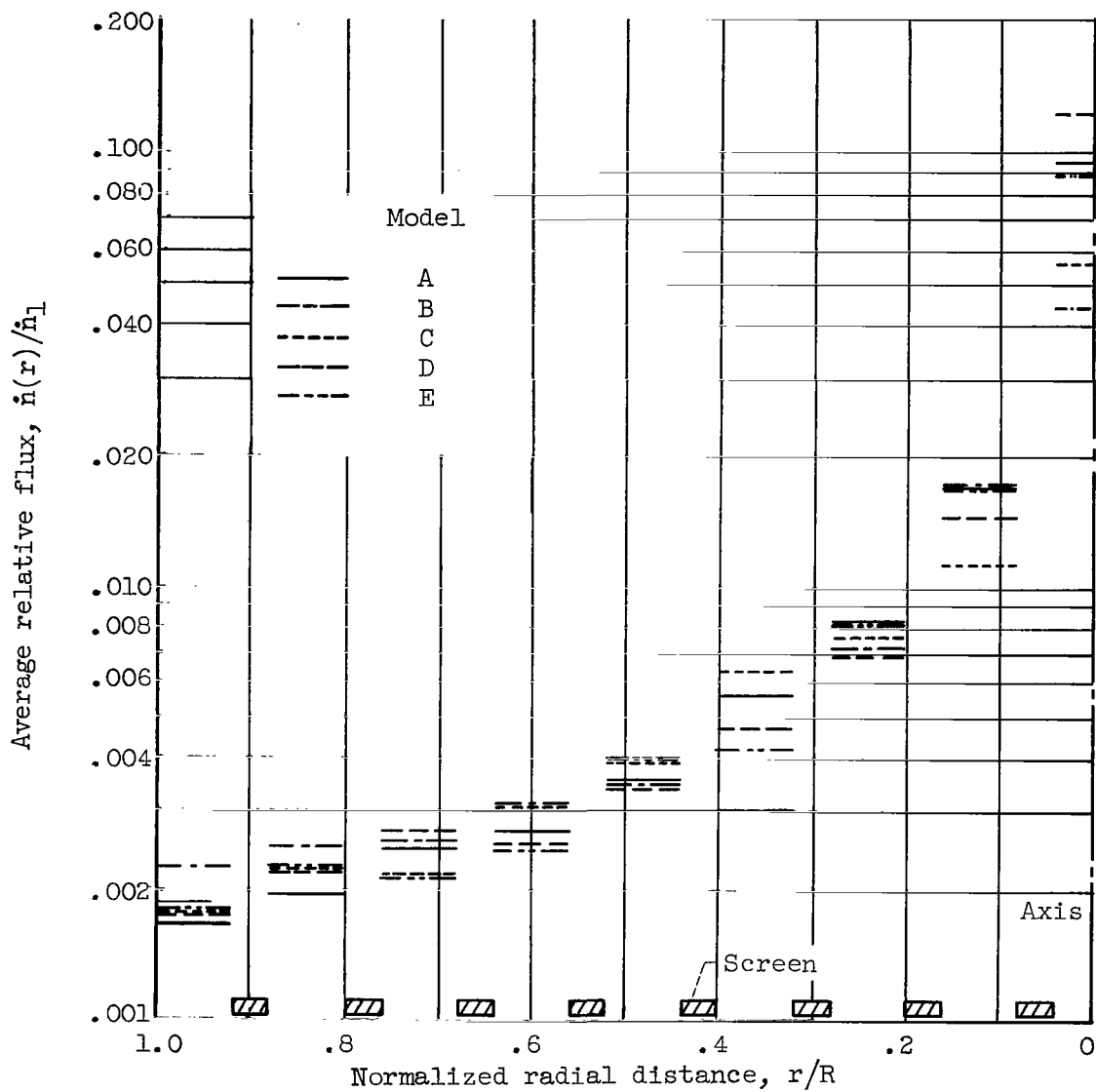


Figure 10. - Average relative radial flux distribution through screen openings. Models from figure 8. Specular reflection.